Walking technicolor in light of Z' searches at the LHC

Alexander Belyaev,[1,3] Azaria Coupe,[1] Mads Frandsen,[2] Emmanuel Olaiya,[3] and Claire Shepherd-Themistocleous[3]
[1]*School of Physics and Astronomy, University of Southampton, Highfield, Southampton SO17 1BJ, United Kingdom*
[2]*High Energy Physics Center, University of Southern Denmark, Campusvej 55, DK-5230 Odense M, Denmark*
[3]*Particle Physics Department, Rutherford Appleton Laboratory, Chilton, Didcot, Oxon OX11 0QX, United Kingdom*

(Received 28 June 2018; published 8 March 2019)

We investigate the potential of the Large Hadron Collider (LHC) to probe one of the most compelling beyond the Standard Model frameworks—walking technicolor (WTC), involving strong dynamics and having a slowly running (walking) new strong coupling. For this purpose we use recent LHC Run 2 data to explore the full parameter space of the minimal WTC model using dilepton signatures from heavy neutral Z' and Z'' resonances predicted by the model. This signature is the most promising one for discovery of WTC at the LHC for the low-intermediate values of the $\tilde{g}$ coupling—one of the principle parameters of WTC. We have demonstrated complementarity of the dilepton signals from both resonances, established the most up-to-date limit on the WTC parameter space, and provided projections for the LHC potential to probe the WTC parameter space at higher future luminosities and upgraded energy. We have explored the whole four-dimensional parameter space of the model and have found the most conservative limit on the WTC scale M_A above 3 TeV for the low values of $\tilde{g}$, which is significantly higher than previous limits established by the LHC collaborations.

DOI: 10.1103/PhysRevD.99.055004

I. INTRODUCTION

With the discovery of a Higgs boson at the Large Hadron Collider (LHC) [1,2] it has become not only possible but also imperative to discover the true origin of mass in the Universe. The traditional Standard Model (SM) Higgs mechanism of mass generation via spontaneous electroweak symmetry breaking (SEWSB) leads to the hierarchy problem, associated with the large fine-tuning between the EWSB scale and the Planck mass. Several classes of beyond the Standard Model (BSM) theories have been proposed to address the shortcomings of the SM, and one of them is technicolor (TC), which is based on *new strong dynamics* [3,4]. In technicolor, EWSB is generated dynamically by the formation of a chiral condensate under the new strong dynamics, providing a natural scale for mass generation without fine-tuning. Experimental bounds from electroweak precision data (EWPD) disfavor TC models with QCD-like dynamics [5], so modern technicolor models must have a modified strong coupling. Walking technicolor (WTC) [6–11] and its recent developments [12–18] are very compelling BSM candidates for the underlying theory of nature. It has a strong coupling α_{TC} with a very slowly running ("walking") regime between the TC energy scale and high energy extended-TC scale. The lightest scalar resonance of WTC can be identified as the experimentally consistent Higgs boson, whose mass scale is naturally generated and thus does not incur a hierarchy problem [19,20]. WTC also provides a rich phenomenology of composite spin-0 and multiple triplets of composite spin-1 resonances, making this a prime candidate for experimental particle physics searches.

Using LHC Run 1 dilepton data, the ATLAS Collaboration has interpreted experimental limits on a new heavy neutral resonance in the context of the WTC parameter space in Refs. [21,22] using dilepton and HV searches, respectively. These WTC interpretations have been following the phenomenological exploration of WTC parameter space performed in [23] for a two-dimensional (2D) bench mark from the whole four-dimensional (4D) parameter space of the model.

This study makes the next step in exploration of the LHC potential to test WTC. First of all, we perform analysis in the full 4D parameter space of the model. Second, we study the complementarity of the dilepton signals from both heavy neutral vector mesons of WTC and demonstrate

its importance. In this work we focus exclusively on Drell-Yan (DY) processes and provide justification for the single peak analysis of current LHC constraints in the context of this model. Finally, we are establishing here the most up-to-date limit on WTC parameter space from LHC dilepton searches for the whole 4D parameter space of the model, and we give projections for the LHC potential to probe WTC parameter space at higher integrated luminosity in the future.

In Sec. II we discuss the WTC model together with the constraints on its parameter space. In Sec. III we explore the phenomenology of WTC and the LHC potential to probe the model. Finally, in Sec. IV we summarize the results of this work and comment on the future prospects for WTC exploration at the LHC.

II. MINIMAL WALKING TECHNICOLOR MODEL

Throughout this paper we focus on the global symmetry breaking pattern $SU(2)_L \times SU(2)_R \to SU(2)_V$. This pattern is realized by the next to minimal walking technicolor model (NMWT) [12,14,23], which features two Dirac fermions transforming in the two-index symmetric representation of the technicolor gauge group $SU(3)$. However, any technicolor model must feature $SU(2)_L \times SU(2)_R \to SU(2)_V$ as a subgroup breaking pattern of the full symmetry breaking pattern $G \to H$. This is required to ensure mass generation for the W and Z bosons and to preserve an $SU(2)_V$ custodial symmetry in the new strong dynamics sector such as that in the SM Higgs sector.

More generally, theories of composite dynamics with a technicolor limit will feature this as a global symmetry breaking subpattern. Examples are composite Higgs and partially composite Higgs models [24,25] with an underlying four-dimensional realization, e.g., [26–30]. Another example is bosonic technicolor [31–34]. In both partially composite Higgs models and in bosonic technicolor, the Higgs particle is a mixture of an elementary and composite scalar. Some aspects of how the spin-1 resonance phenomenology is affected by aligning the theory away from the technicolor vacuum in composite Higgs, and partially composite Higgs models are given in [28,35]. In general, the mass scale set by the Goldstone boson decay constant of the strong interactions, F_π, is larger in composite Higgs models than in ordinary technicolor while it is smaller in the bosonic technicolor models. In partially composite Higgs models, the scale depends on the relative size of the elementary doublet vacuum expectation value (VEV) v and the vacuum alignment angle θ. In general F_π in these different composite models is determined through a constraint of the form

$$v_{\mathrm{EW}}^2 = F_\pi^2 N_D \sin^2\theta + v^2, \tag{1}$$

where N_D is the number of electroweak doublet fermion families, $\theta = \pi/2$ corresponds to the technicolor vacuum, and $0 < \theta < \pi/2$ corresponds to the composite Higgs vacuum.

In this study we restrict ourselves to the technicolor limit, which provides dynamical electroweak symmetry breaking and a composite Higgs resonance, but requires a further extension to provide SM fermion masses. The composite Higgs resonance has been argued to be heavy in the technicolor limit with respect to the electroweak scale, by analogy with scalar resonances in QCD which are heavy compared to the QCD pion decay constant. However, for composite sectors that are not a copy of QCD it is a nonperturbative problem to determine the lightest scalar mass. Both model computations [14,36] and lattice simulations [37,38] of models such as the NMWT model, which appear to be near the conformal window, have indicated the presence of a scalar 0^{++} resonance that is much lighter than expected from simply scaling up scalar masses in QCD. The physics behind the origin of the fermion masses can also play a role in reducing this TC Higgs mass to the observed value at LHC and at the same time provide SM Higgs-like couplings [19,20] to the SM particles. It is possible to probe the origin of the fermion masses, whether they are due to extended technicolor, fermion partial compositeness, or a new elementary scalar, via the pseudoscalar sector of the theory, the analogues of the QCD η and η' resonances as discussed in [39,40].

We follow the same prescription for constructing an effective theory of the underlying composite dynamics as in [23,41] by introducing composite spin-1 resonances transforming under the $SU(2)_L \times SU(2)_R$ global symmetry: Two new triplets of heavy spin-1 resonances are introduced at interaction eigenstate level $A_{L/R}$ as gauge fields under $SU(2)_{L/R}$, respectively. The $SU(2)_L$ is gauged as $SU(2)_W$ such that the A_L fields form a weak triplet analogous to the triplet in W' models while the A_R fields are $SU(2)_W$ singlets.

Together with the Standard Model electroweak fields in the gauge eigenbasis, $\tilde{W}_\mu$ and $\tilde{B}_\mu$, we define chiral fields $C_{L/R\mu}$,

$$C_{L\mu} \equiv A_{L\mu} - \frac{g}{\tilde{g}}\tilde{W}_\mu, \qquad C_{R\mu} \equiv A_{R\mu} - \frac{g'}{\tilde{g}}\tilde{B}_\mu, \tag{2}$$

where g and g' are the usual Standard Model EW coupling constants and $\tilde{g}$ is the coupling constant of the NMWT gauge interactions. These fields transform homogeneously when the $A_{L/R}$ fields are introduced formally as gauge fields.

The scalar composite Higgs resonance H and the triplet of pions π^a absorbed by the W and Z bosons are introduced as a bidoublet field under the $SU(2)_{L/R}$ symmetries described via the 2×2 matrix M,

$$M = \frac{1}{\sqrt{2}}[v + H + 2i\pi^a T^a],$$
$$M \to u_L M u_R^\dagger, \qquad u_{L/R} \in SU(2)_{L/R}, \tag{3}$$

where $a = 1, 2, 3$, $v = \mu/\sqrt{\lambda}$ is the vacuum expectation value associated with the breaking of the chiral symmetry, and T^a are the generators of the $SU(2)$ groups, related to the Pauli matrices by $T^a = \sigma^a/2$. The electroweak covariant derivative of M is

$$D_\mu M = \partial_\mu M - ig\tilde{W}^a_\mu T^a M + ig' M \tilde{B}_\mu T^3. \tag{4}$$

With these definitions we write the low-energy effective Lagrangian of the model, up to dimension-four operators as in [23]

$$\begin{aligned}\mathcal{L}_{\text{boson}} = &-\frac{1}{2}\text{Tr}[\tilde{W}_{\mu\nu}\tilde{W}^{\mu\nu}] - \frac{1}{4}\tilde{B}_{\mu\nu}\tilde{B}^{\mu\nu} - \frac{1}{2}\text{Tr}[F_{L\mu\nu}F_L^{\mu\nu} + F_{R\mu\nu}F_R^{\mu\nu}] + m^2\text{Tr}[C_{L\mu}^2 + C_{R\mu}^2] + \frac{1}{2}\text{Tr}[D_\mu M D^\mu M^\dagger] \\ &- \tilde{g}^2 r_2 \text{Tr}[C_{L\mu} M C_R^\mu M^\dagger] - \frac{i\tilde{g}r_3}{4}\text{Tr}[C_{L\mu}(MD^\mu M^\dagger - D^\mu M M^\dagger) + C_{R\mu}(M^\dagger D^\mu M - D^\mu M^\dagger M)] \\ &+ \frac{\tilde{g}^2 s}{4}\text{Tr}[C_{L\mu}^2 + C_{R\mu}^2]\text{Tr}[MM^\dagger] + \frac{\mu^2}{2}\text{Tr}[MM^\dagger] - \frac{\lambda}{4}\text{Tr}[MM^\dagger]^2,\end{aligned} \tag{5}$$

where $\tilde{W}_{\mu\nu}$ and $\tilde{B}_{\mu\nu}$ are the SM electroweak field strength tensors and $F_{L/R\mu\nu}$ are the field strength tensors corresponding to the vector meson fields.

The global symmetry breaking pattern $SU(2)_L \times SU(2)_R \times U(1)_V \to SU(2)_V \times U(1)_V$ is triggered by the VEV of M and provides the 3 Goldstone degrees of freedom for the massive W and Z bosons. The heavy vector resonances, here introduced via the $A_{L/R}$ triplets, can equivalently be treated as Higgs'ed gauge fields of a "hidden local symmetry" copy of the above global symmetry group [42], as discussed in [18]. The physical spectrum of the model then consists of the two triplets of spin-1 mesons, which in the absence of electroweak interactions form a vector triplet V under $SU(2)_V$ and the axial-vector partner triplet A, analogous to the ρ and a_1 vector mesons in QCD. In this study we focus on the two neutral resonance mass eigenstates which, in the presence of SM electroweak interactions, we for convenience refer to as Z' and Z'' although these are distinct from sequential Z' resonances.

The spin-1 sector of the Lagrangian in Eq. (5) contains five parameters, m, $\tilde{g}$, r_2, r_3, and s. The masses and decay constants of the vector and axial-vector resonances, in the limit of zero electroweak couplings, are given in terms of these parameters as

$$\begin{aligned} M_V^2 &= m^2 + \frac{\tilde{g}^2(s - r_2)v^2}{4}, & F_V &= \frac{\sqrt{2}M_V}{\tilde{g}}, \\ M_A^2 &= m^2 + \frac{\tilde{g}^2(s + r_2)v^2}{4}, & F_A &= \frac{\sqrt{2}M_A}{\tilde{g}}\chi, \end{aligned} \tag{6}$$

where

$$\chi \equiv 1 - \frac{v^2\tilde{g}^2 r_3}{4M_A^2}. \tag{7}$$

The technipion decay constant F_π may be expressed in terms of F_V and F_A as

$$F_\pi^2 = (1 + 2\omega)F_V^2 - F_A^2, \tag{8}$$

with

$$\omega \equiv \frac{v^2\tilde{g}^2}{4M_V^2}(1 - r_3 + r_2) \tag{9}$$

and with $F_\pi = 246\sqrt{N_D}$ GeV in technicolor models with N_D families of technifermions and no elementary doublet scalars. Here we assume $N_D = 1$ as in the NMWT model. We can now make use of the Weinberg sum rules (WSRs) [43] to constrain the number of parameters in the effective model and connect them to the underlying fermionic dynamics.

The assumed asymptotic freedom of the effective theory implies the first and second WSRs, respectively,

$$\int_0^\infty ds \text{Im}\Pi_{LR}(s) = 0, \quad \int_0^\infty ds s \text{Im}\Pi_{LR}(s) = 0, \tag{10}$$

where $\Pi_{LR}(s)$ is the Lorentz invariant part of the LR correlation function:

$$\Pi^{a,b}_{\mu\nu LR}(q) = (q_\mu q_\nu - g_{\mu\nu}q^2)\delta^{ab}\Pi_{LR}(q^2), \tag{11}$$

with

$$i\Pi^{a,b}_{\mu\nu LR}(q) = \int d^4x e^{iq\cdot x}[\langle J^a_{\mu,V}(x)J^b_{\nu,V}(0)\rangle - \langle J^a_{\mu,A}(x)J^b_{\nu,A}(0)\rangle]. \tag{12}$$

Assuming that only the lowest spin-1 resonances A, V saturate the WSRs, the vector and axial vector spectral densities are given in terms of the spin-1 masses and decay constants as

$$\begin{aligned} \text{Im}\Pi_V(s) &= \pi F_V^2 \delta(s - M_V^2), \\ \text{Im}\Pi_A(s) &= \pi F_\pi^2 \delta(s) + \pi F_A^2 \delta(s - M_A^2). \end{aligned} \tag{13}$$

The first WSR therefore implies that $\omega = 0$ and

$$F_V^2 - F_A^2 = F_\pi^2. \tag{14}$$

In terms of the Lagranian parameter this gives the relation

$$r_2 = r_3 - 1. \tag{15}$$

The second WSR is less dominated by the infrared dynamics than the first WSR as seen from Eq. (10). We therefore allow for a modification of the second WSR encoded by the dimensionless parameter a following [44]

$$a\frac{8\pi^2}{d(R)}F_\pi^4 = F_V^2 M_V^2 - F_A^2 M_A^2, \tag{16}$$

where $d(R)$ is the dimension of the gauge group representation of the underlying technifermions. The parameter a measures the contribution of the underlying dynamics to the integral in Eq. (10) from intermediate energies, above the confinement scale.

Finally the electroweak Peskin-Takeuchi S parameter is related to a zeroth Weinberg sum rule,

$$S = 4\int_0^\infty \frac{ds}{s}\mathrm{Im}\bar{\Pi}_{LR} = 4\pi\left[\frac{F_V^2}{M_V^2} - \frac{F_A^2}{M_A^2}\right]. \tag{17}$$

Combining the first and second WSRs it follows that the a parameter gives a negative contribution to axial-vector mass difference $M_A^2 - M_V^2$ and a negative contribution to the S parameter. We therefore expect a to be positive in a near conformal theory yielding a smaller S-parameter and a more degenerate axial-vector mass spectum than in QCD. This is in line with, e.g., model computations [36,45] based on Schwinger-Dyson analysis, but here we take it as an assumption.

In QCD we expect $a \simeq 0$ while in near-conformal theories, where the coupling constant is assumed to be approximately constant in a region above the confinement scale, we expect $a > 0$ [44].

This allows us to trade one of the Lagrangian parameters for the S parameter via the relation

$$S = \frac{8\pi}{\tilde{g}^2}(1 - \chi^2). \tag{18}$$

We are left with a four-dimensional parameter space that describes the model: M_A, $\tilde{g}$, S, s. The Lagrangian constant s parametrizes the interactions of the technicolor spin-1 mesons with the Higgs sector [see Eq. (5)]. Since we do not consider the composite Higgs phenomenology, the only relevant effect of the s parameter is on the branching ratio of the Z' and Z'' states into dileptons. The branching ratios into dileptons are maximal for $s = 0$, so we therefore restrict to this throughout. This leaves three relevant parameters

$$M_A, \qquad \tilde{g}, \qquad S. \tag{19}$$

We show the value of the a parameter in the M_A, $\tilde{g}$ plane for different values of S in Fig. 1. Restricting to positive values of a we get an upper limit on the mass parameter M_A that complements the experimental limits we derive from dilepton searches.

III. PHENOMENOLOGY AND LHC POTENTIAL TO PROBE WTC PARAMETER SPACE

In our analysis of heavy neutral spin-1 resonances in the NMWT parameter space, we conduct a three-dimensional scan over M_A, $\tilde{g}$, and S. The results in this section are presented in the M_A, $\tilde{g}$ parameter space for discrete values of S such as $S = -0.1, 0.0, \ldots, 0.3$. The largest value, $S = 0.3$ for the range we choose, is already disfavored by EWPD [46]; however, we include it in this work for direct comparison to results of the previous work [23]. The remaining limits of the scan over S ensure that the tension with EWPD is minimized (for the zero T parameter). In this section we present results at the benchmark $S = 0.1$; fixed values of $S \neq 0.1$ are given in the Appendix A 4.

There is an upper bound on $\tilde{g}$,

$$\tilde{g} < \sqrt{\frac{8\pi}{S}}, \tag{20}$$

which follows from Eq. (17) and ensures that all physical quantities are real as we will see below. For $S = 0.3$, the biggest value of S we consider here, the upper limit is $\tilde{g} = 9.15$. Therefore we present all results in the M_A, $\tilde{g}$ space with $\tilde{g} \leq 9$ to avoid unphysical parameter space.

The phenomenology of the NMWT model is explored using the CalcHEP package [47], which allows one to perform simple and robust analysis of tree-level collider events. The Lagrangian for NMWT was implemented using LanHEP [48], from which all interaction vertices are generated for use in CalcHEP. We focus on neutral heavy spin-1 resonances in the Drell-Yan channel, with dileptons' signature. The mass spectra of the Z'/Z'' are presented in Sec. III A 1, the coupling strength of Z'/Z'' vertices in Sec. III A 2, followed by a discussion of the total widths and dilepton branching ratios in Sec. III B; production and total cross sections for DY processes of Z'/Z'' are given in Sec. III C; Sec. III D explores the interference between the neutral resonances and discusses the validity of reinterpreting LHC constraints for the NMWT model; and finally, Sec. III E explores the LHC potential to probe the WTC parameter space.

A. Masses and couplings

1. Mass spectra

Besides numerical analysis it is informative also to perform an analytical one as we do for some masses and

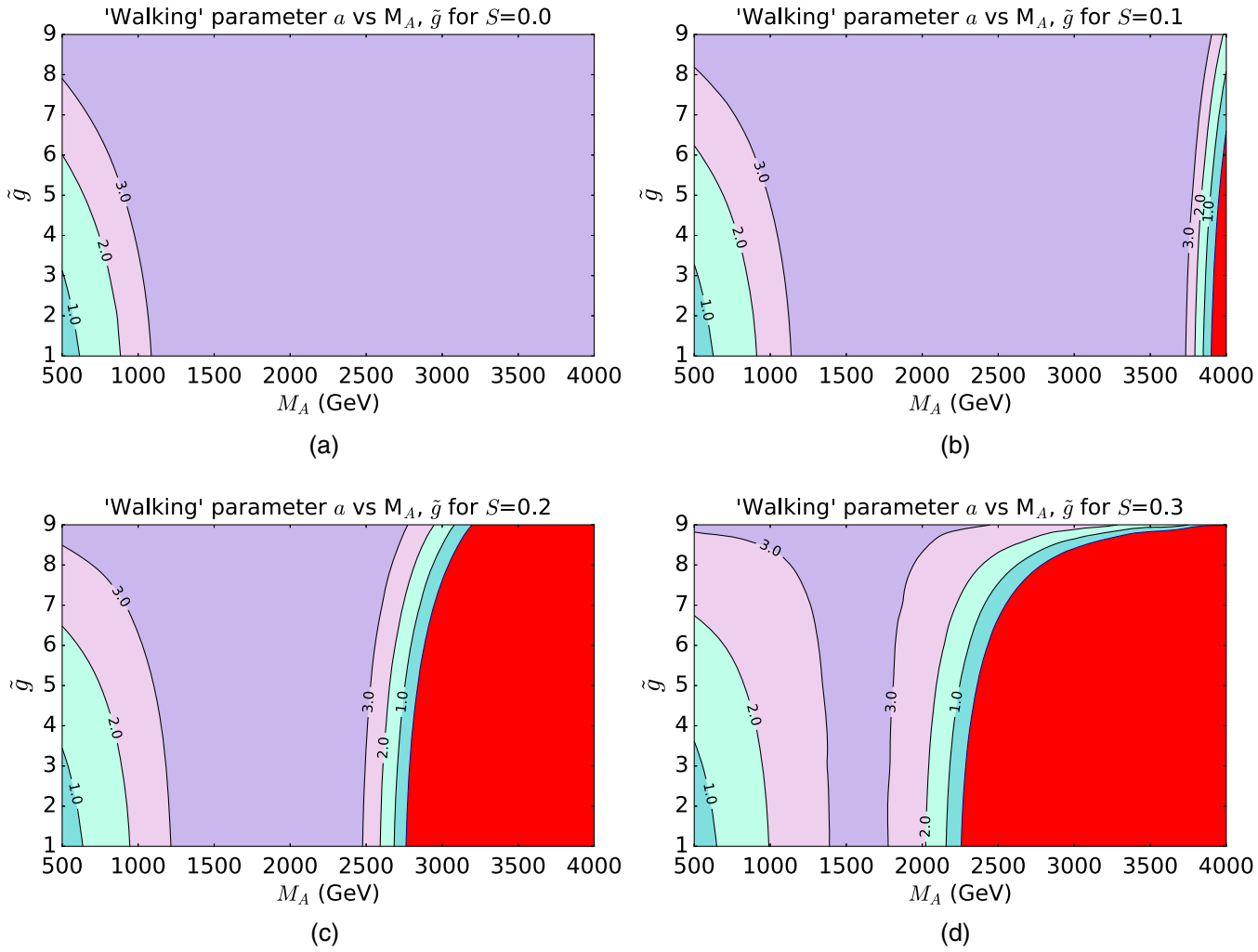

FIG. 1. Contour levels for a parameter in $(M_A, \tilde{g})$ NMWT plane for various values of S and fixed $s = 0$. The red-shaded region corresponds to excluded $a < 0$ space.

couplings to understand the qualitative properties of the model and the limits of the parameter space. Diagonalizing the neutral mixing matrix (see details in the Appendix A 1), we find the Z'/Z'' masses to second order in $\tilde{g}^{-1}$ take the form

$$M_{Z'}^2 = M_A^2\left(1 + \frac{g_1^2 + g_2^2}{\tilde{g}^2}\chi^2\right), \tag{21}$$

$$M_{Z''}^2 = M_A^2\left(1 + \frac{g_1^2 + g_2^2}{2\tilde{g}^2}\right)\left(\chi^2 + \frac{\tilde{g}^2 F_\pi^2}{2M_A^2}\right), \tag{22}$$

where from Eq. (18) we express χ as

$$\chi = \sqrt{1 - \frac{S\tilde{g}^2}{8\pi}}, \tag{23}$$

and $U(1)_Y$ and $SU(2)_L$ couplings g_1 and g_2 are functions of $(M_A, \tilde{g}, S)$; see Eqs. (A26) and (A25). Both g_1 and g_2 have a very mild dependence on the model parameters.[1]

One should note that in general $Z - Z'$ and $Z - Z''$ mixing plays a very important role in constraining BSM models. In case of just extra $U(1)'$ theory with one Z' boson the $Z - Z'$ mixing is constrained to be below about 10^{-3} by the EWPD; see, e.g., [49] and references therein. In case of the NMWT model under study with the embedded $SU(2)_V$ custodial symmetry, the electroweak precision parameters (EWPP) are under control, including the S parameter, which is chosen to be an explicit model parameter. In the NMWT model the $Z - Z'$ and $Z - Z''$ mixings, for example, are as large as 10^{-2} as one can explicitly find using the mixing matrix given by Eq. (41) of

[1]Variation in the couplings is less than 1% level across the parameter space.

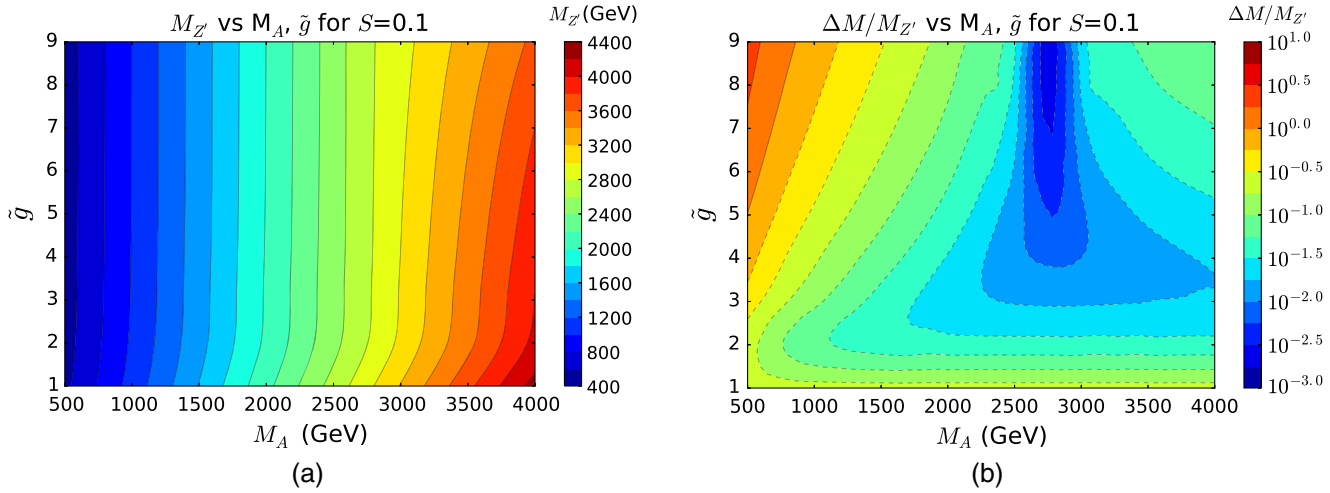

FIG. 2. (a) $M_{Z'}$ (GeV) (b) $\Delta M/M_{Z'}$ as a function of M_A, $\tilde{g}$, at benchmark values of $S = 0.1$ and $s = 0$.

the Appendix A 1. However, the size of the EWPP is actually defined by the WWZ', WWZ'', $W'WZ$, etc., couplings, which are as small as 10^{-3} or below because of the cancellation and the interplay between the $Z - Z'$, $Z - Z''$, $W - W'$, and $W - W''$ mixings due to the custodial symmetry of the theory.

The mass spectrum of the Z' is shown in Fig. 2(a) and numerically presented in Table I where we also present the Z'' mass for the 3D grid in $(M_A, \tilde{g}, S)$ space. One can see that for $\tilde{g} \gtrsim 2$, $M_{Z'} \simeq M_A^2$ as follows from Eq. (21). In Fig. 2(b) we present the spectrum for the relative mass difference, $\Delta M/M_{Z'}$, where $\Delta M = M_{Z''} - M_{Z'}$. One can see that $M_{Z''}$ behavior is less trivial, which reflects the "competition" of $\tilde{g}$ and F_π/M_A ratios in Eq. (22). For large M_A one can observe that Z' starts to mildly depend on $\tilde{g}$. This change in behavior is due to a change of state of the $Z'(Z'')$ from mostly axial (vector) to mostly vector (axial) [23]. Figure 2(b) clearly reflects this mass inversion for $\tilde{g} > 1$ at a fixed $M_{\rm inv} = M_A$, which to second order in $\tilde{g}^{-1}$ takes the form

$$M_{\rm inv}^2 = \left(1 + \frac{g_1^2 + g_2^2}{\tilde{g}^2}\right)\frac{4\pi}{S}F_\pi^2. \tag{24}$$

Using the benchmark $S = 0.1$, the mass inversion occurs at $M_A = 2760$ GeV, and we clearly observe this behavior in Fig. 2(b).

The mass splitting is large at low M_A and high $\tilde{g}$, opening new decay channels such as $Z'' \to W^{+\prime}W^{-\prime}$. This is discussed further in Sec. III B.

2. Couplings

Here we explore the analytic forms of Z' and Z'' couplings to fermions. These are composed of elements of the neutral diagonalization matrix N_{ij} [18], and details of the mixing matrix calculation are included in the Appendix A 1.

For the vertices with fermions, the coupling strengths can be decomposed into left- and right-handed parts and to second order in $1/\tilde{g}$, and $g_{Z'f\bar{f}}$ and $g_{Z''f\bar{f}}$ couplings take the form

$$g^L_{Z'f\bar{f}} = \frac{\chi}{2\sqrt{2}\tilde{g}}(-I_3 g_2^2 + Y g_1^2),\quad g^R_{Z'f\bar{f}} = \frac{\chi}{2\sqrt{2}\tilde{g}} q_f g_1^2, \tag{25}$$

$$g^L_{Z''f\bar{f}} = \frac{1}{2\sqrt{2}\tilde{g}}(I_3 g_2^2 + Y g_1^2),\quad g^R_{Z''f\bar{f}} = \frac{1}{2\sqrt{2}\tilde{g}} q_f g_1^2, \tag{26}$$

where $I_3 = \pm 1/2$ is the usual third component of the weak isospin for up and down fermions, respectively,

TABLE I. Masses of the neutral resonances at reference points in the M_A, $\tilde{g}$, S parameter space, displayed in the format $M_{Z'}$ ($M_{Z''}$) in GeV for each parameter space value.

		M_A [GeV]			
S	$\tilde{g}$	1000	1500	2000	2500
−0.1	1	1080(1339)	1614(1984)	2148(2639)	2683(3296)
	3	1016(1163)	1523(1640)	2030(2138)	2536(2643)
	5	1006(1370)	1509(1808)	2012(2283)	2515(2778)
	7	1003(1642)	1505(2049)	2007(2510)	2508(3001)
	9	1002(1947)	1503(2334)	2005(2788)	2506(3280)
0.1	1	1078(1325)	1610(1976)	2144(2629)	2678(3283)
	3	1015(1130)	1520(1590)	2023(2071)	2522(2565)
	5	1005(1295)	1507(1678)	2010(2100)	2511(2543)
	7	1002(1518)	1503(1821)	2004(2175)	2505(2560)
	9	1001(1773)	1502(1998)	2002(2277)	2503(2591)
0.3	1	1075(1320)	1607(1968)	2139(2618)	2672(3270)
	3	1013(1097)	1514(1541)	1985(2034)	2452(2540)
	5	1004(1215)	1505(1537)	1898(2008)	2280(2510)
	7	1001(1382)	1502(1560)	1779(2002)	2025(2503)
	9	1000(1580)	1500(1593)	1611(2000)	1634(2500)

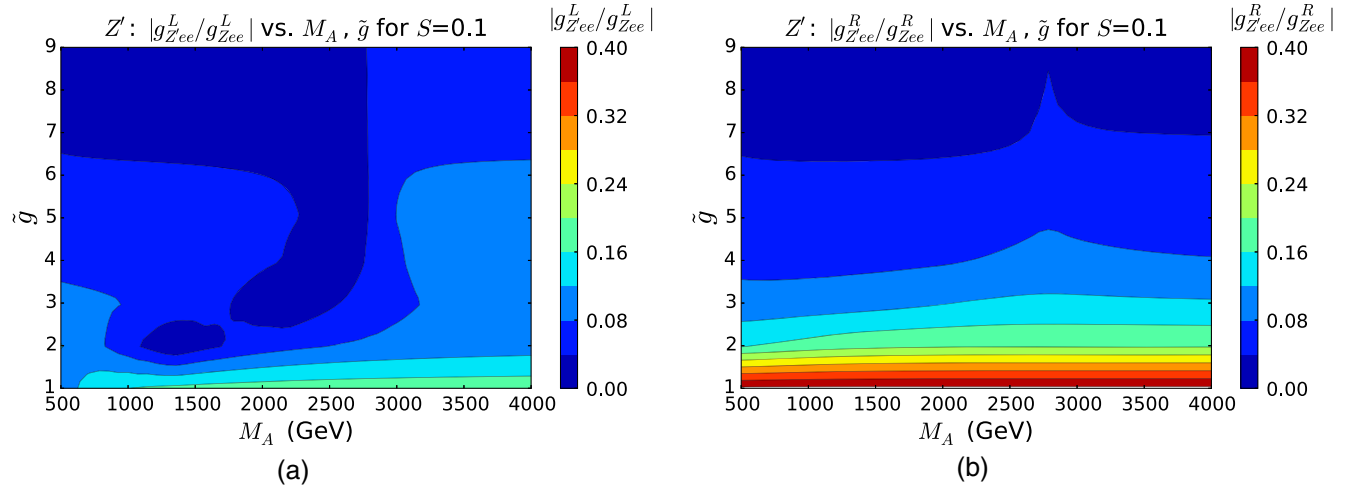

FIG. 3. Coupling of Z' to charged lepton pairs as a ratio to its SM equivalent separated into left- and right-handed components, (a) $|g^L_{Z'l^+l^-}/g_{Zl^+l^-}|$, (b) $|g^R_{Z'l^+l^-}/g_{Zl^+l^-}|$, as a function of M_A and $\tilde{g}$ parameters at the benchmark values of $S = 0.1$ and $s = 0$.

$Y = q_f - I_3$ is their hypercharge, and q_f is the charge of the fermions.

The parameter dependence of the Z' and Z'' dilepton couplings are given as a ratio to the SM $g_{Zl^+l^-}$ in Figs. 3 and 4, respectively. Both L and R components of the Z' dilepton coupling increase as $\tilde{g} \to 1$; however, as the coupling is diluted through the mixing effects between the gauge fields, $g_{Z'l^+l^-} \geq g_{Zl^+l^-}$ is never realized.

Similarly, the L component of the Z'' dilepton coupling grows as $\tilde{g} \to 1$; however, this is not the case for the R component. The R component is suppressed in comparison to the Z' as the mixing with the photon is smaller for $\gamma - Z''$ than for $\gamma - Z'$; such mixing effects are discussed further in Sec. III B.

Again we see that the axial (vector) composition of the Z' (Z'') affects both L and R coupling strengths, suppressing the coupling as the Z' (Z'') becomes mostly vector (axial).

B. Widths and branching ratios

The width-to-mass ratio Γ/M for Z' and Z'' is shown in Fig. 5.

One can see that Z' is generically narrow in the whole parameter space—the Γ/M is always below 10%. One should also note that for large values of $\tilde{g}$ and $M_A < M_{\text{inv}}$ the main contribution to the width is coming from $Z' \to ZH$ decay as one can see from Figs. 6(a) and 6(b) where we present (a),(b) $\text{Br}(Z')$ and (c),(d) $\text{Br}(Z'')$ for all decay channels as a function of M_A at the fixed values of (a),(c) $\tilde{g} = 3$ and (b),(d) $\tilde{g} = 8$, at benchmark values of $S = 0.1$ and $s = 0$. This happens because of the following asymptotic of $g_{Z'ZH}$ coupling at large $\tilde{g}$:

$$g_{Z'ZH} = -\frac{\tilde{g}^2 v}{16}\sqrt{\frac{(g_2^2 + g_1^2)S}{\pi}}, \tag{27}$$

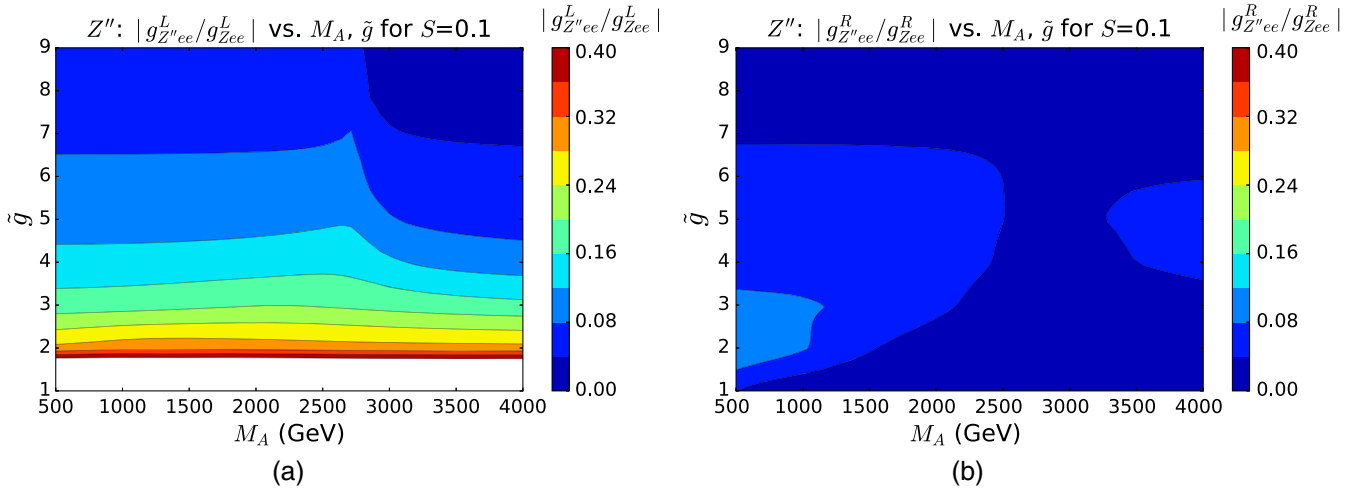

FIG. 4. Coupling of Z'' to charged lepton pairs as a ratio to its SM equivalent separated into left- and right-handed components, (a) $|g^L_{Z''l^+l^-}/g_{Zl^+l^-}|$, (b) $|g^R_{Z''l^+l^-}/g_{Zl^+l^-}|$, as a function of M_A and $\tilde{g}$ parameters at the benchmark values of $S = 0.1$ and $s = 0$.

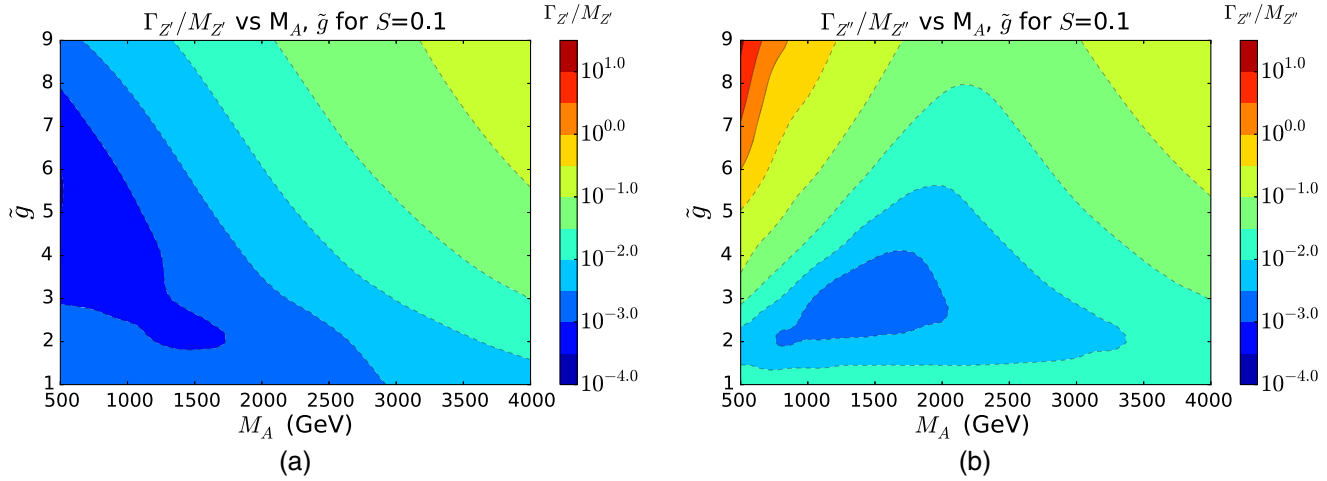

FIG. 5. (a) $\Gamma_{Z'}/M_{Z'}$. (b) $\Gamma_{Z''}/M_{Z''}$ as a function of M_A and $\tilde{g}$ parameters at benchmark values of $S = 0.1$ and $s = 0$.

which makes $\Gamma(Z')$ increase with the increase of $\tilde{g}$. One can see the numerical results confirming this effect in Table II, where we present $\Gamma(Z')$ and $\Gamma(Z'')$ for the 3D grid in $(M_A, \tilde{g}, S)$ space.

For $M_A > M_{\text{inv}}$, Z' "switches" its properties from pseudovector to vector, and its width is enhanced then by the $Z' \to W + W-$ decay for large $\tilde{g}$ with the respective $g_{Z'WW}$ coupling proportional to $\tilde{g}$. In the region of low values of $\tilde{g}$

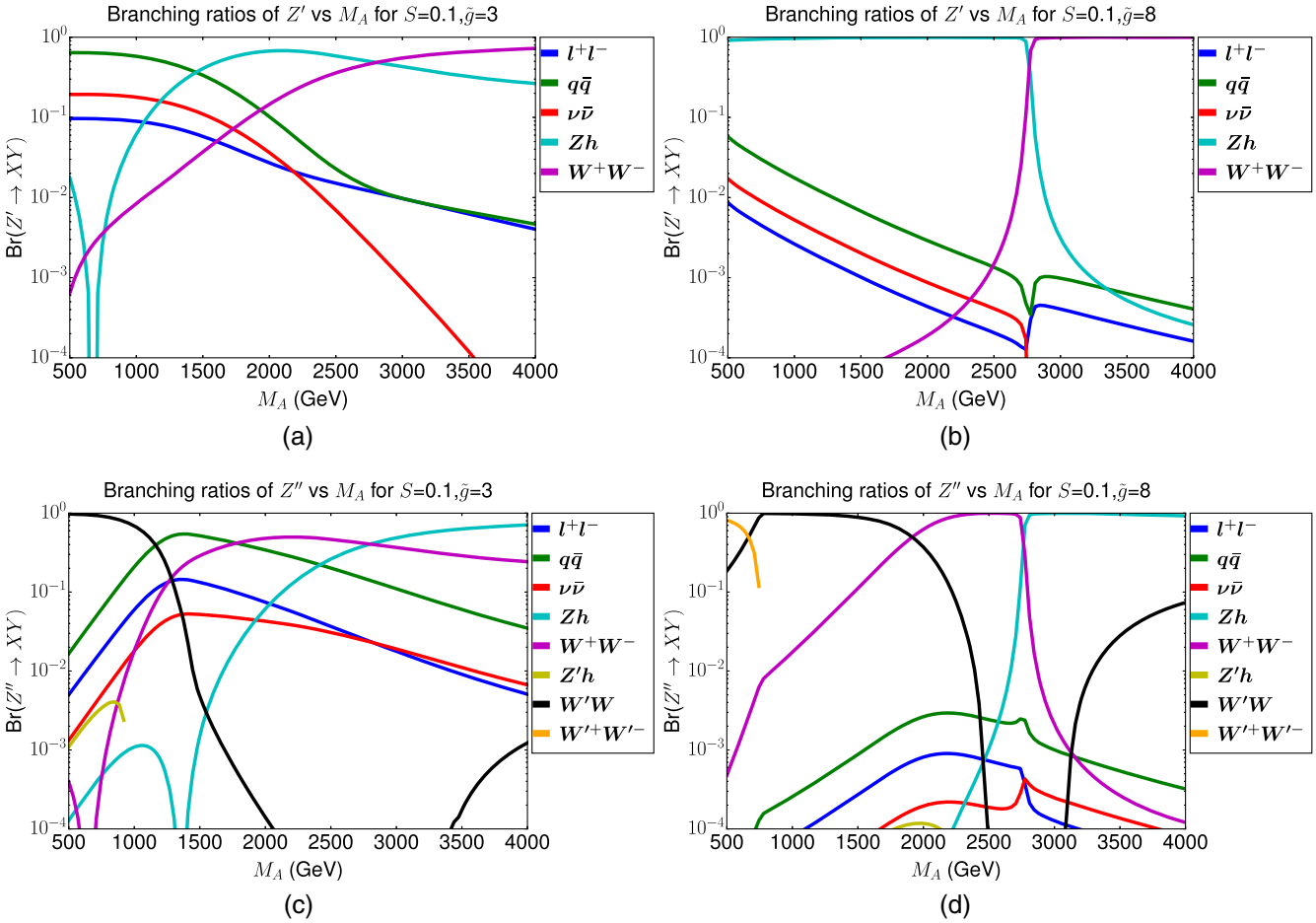

FIG. 6. (a),(b) Br(Z') and (c),(d) Br(Z'') for all decay channels as a function of M_A at the fixed values of (a) $\tilde{g} = 3$, (b) $\tilde{g} = 8$, at benchmark values of $S = 0.1$ and $s = 0$.

TABLE II. Widths of the neutral resonances in the M_A, $\tilde{g}$, S parameter space, displayed in the format $\Gamma_{Z'}$ ($\Gamma_{Z''}$) in GeV for each parameter space value.

		M_A [GeV]			
S	$\tilde{g}$	1000	1500	2000	2500
−0.1	1	2.91(35.28)	4.54(52.92)	6.68(72.28)	9.76(94.34)
	3	1.29(10.79)	2.92(7.73)	7.20(12.28)	17.39(24.99)
	5	1.37(180.97)	5.10(117.65)	16.44(110.57)	44.28(143.36)
	7	2.89(932.69)	11.15(691.70)	35.46(648.36)	93.58(742.68)
	9	6.75(3028.96)	23.56(2435.70)	69.88(2375.84)	176.01(2685.93)
0.1	1	2.72(33.70)	4.02(48.98)	5.50(64.11)	7.50(79.44)
	3	0.88(4.13)	1.80(2.69)	4.74(6.40)	12.93(15.07)
	5	0.79(76.29)	3.60(19.00)	12.85(14.75)	36.46(36.86)
	7	1.99(350.34)	8.64(109.07)	28.30(46.82)	75.39(76.16)
	9	5.66(899.79)	19.44(328.60)	55.33(124.77)	134.68(135.22)
0.3	1	2.70(32.48)	4.62(47.28)	8.91(64.77)	19.03(90.61)
	3	1.87(2.75)	9.37(10.55)	34.98(37.18)	99.34(107.84)
	5	5.53(30.22)	27.87(27.69)	79.15(97.60)	197.15(288.29)
	7	18.16(108.87)	64.34(59.34)	113.87(195.62)	217.11(580.30)
	9	72.97(125.19)	160.17(109.98)	116.31(318.94)	124.76(617.72)

and not so large values of M_A the contribution from $Z' \to f\bar{f}$ also plays an important role. This also happen for small values of $S \simeq 0$ as one can see from Figs. 20 and 21 in the Appendix A, where we present additional plots for $S = -0.1$, 0, 0.2, and 0.3. From Fig. 5 one can see that the picture of the width-to-mass ratio for Z'' is qualitatively different from the one for Z': though the Γ/M is also below 10% for $\tilde{g} \lesssim 5$, for bigger values of $\tilde{g}$ the Γ/M becomes very large especially in the small M_A region where $\tilde{g}$-enhanced $Z'' \to W'W'$ decay opens for vector Z'', or for large values of M_A where $\tilde{g}$-enhanced $Z'' \to ZH$ decay opens for pseudovector Z'' (see Fig. 6 as well as analogous Figs. 20 and 21 from the Appendix A 5 b). In this region Z'' does not contribute to the dilepton signature at the LHC, and therefore this region can safely be explored and interpreted using Z' dilepton signature at the LHC.

Let us take a closer look at the dilepton signature and the respective Z' and Z'' branching ratios in 2D (M_A, $\tilde{g}$) parameter space, presented in Fig. 7 for $S = 0.1$ and Table III presenting numerical values for $\mathrm{Br}(Z' \to e^+e^-)$ and $\mathrm{Br}(Z'' \to e^+e^-)$ for the 3D grid in $(M_A, \tilde{g}, S)$ space. Besides an expected $1/\tilde{g}$ suppression, in Fig. 7 one can observe that for low values of $\tilde{g}$ both $\mathrm{Br}(Z' \to \ell^+\ell^-)$ and $\mathrm{Br}(Z'' \to \ell^+\ell^-)$ are enhanced above the 3% value corresponding to $\mathrm{Br}(Z \to \ell^+\ell^-)$ in SM. One can see from Table III that, for example, for $M_A = 1500$ GeV, $S = 0.1$ and $\tilde{g} = 1$ $\mathrm{Br}(Z' \to e^+e^-) \simeq 12.3\%$ which is about 4 times bigger than the SM value. This enhancement is related to a

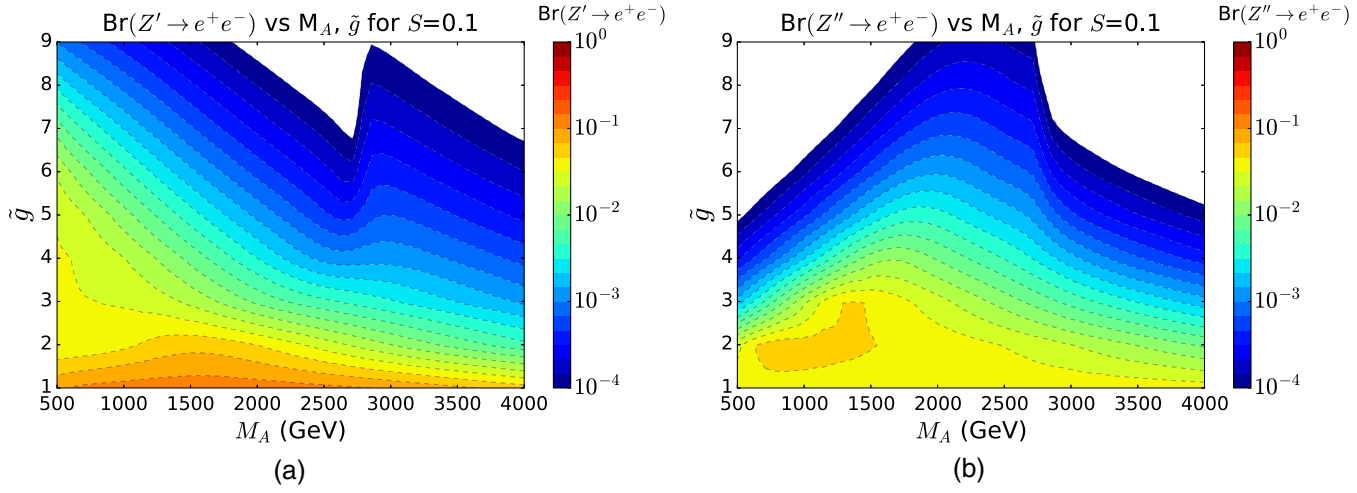

FIG. 7. (a) $\mathrm{Br}(Z' \to e^+e^-)$. (b) $\mathrm{Br}(Z'' \to e^+e^-)$ as a function of M_A and $\tilde{g}$ parameters at benchmark values of $S = 0.1$ and $s = 0$.

TABLE III. Dielectron branching fraction of Z', Z'' in the M_A, $\tilde{g}$, S parameter space, displayed in the format $\mathrm{Br}(Z' \to e^+e^-)$ $[\mathrm{Br}(Z'' \to e^+e^-)]$ in %.

		M_A [GeV]			
S	$\tilde{g}$	1000	1500	2000	2500
−0.1	1	10.941(3.963)	10.759(3.873)	9.854(3.749)	8.467(3.576)
	3	2.226(0.782)	1.377(1.572)	0.704(1.313)	0.350(0.807)
	5	0.827(0.019)	0.327(0.038)	0.134(0.052)	0.061(0.049)
	7	0.217(0.002)	0.083(0.004)	0.035(0.005)	0.016(0.005)
	9	0.062(0.000)	0.026(0.001)	0.012(0.001)	0.006(0.001)
0.1	1	11.788(4.080)	12.280(4.112)	12.084(4.154)	11.119(4.174)
	3	2.986(1.991)	1.930(4.455)	0.903(2.487)	0.502(1.229)
	5	1.171(0.042)	0.373(0.220)	0.133(0.360)	0.050(0.183)
	7	0.211(0.005)	0.072(0.021)	0.029(0.058)	0.013(0.043)
	9	0.038(0.001)	0.016(0.005)	0.008(0.014)	0.004(0.015)
0.3	1	11.988(4.162)	10.784(4.186)	7.532(4.040)	4.429(3.595)
	3	1.255(2.910)	0.356(1.077)	0.301(0.233)	0.147(0.085)
	5	0.129(0.099)	0.033(0.142)	0.058(0.016)	0.028(0.006)
	7	0.012(0.016)	0.005(0.033)	0.019(0.002)	0.012(0.001)
	9	0.000(0.009)	0.000(0.011)	0.010(0.000)	0.010(0.000)

quite subtle effect that does not follow from Eq. (25), which is valid for intermediate-large values of $\tilde{g}$; for $\tilde{g} \simeq 1$ one can check numerically that photon-Z' mixing is enhanced, while $Z - Z'$ is suppressed, which leads to a relative suppression of $\mathrm{Br}(Z' \to \nu\nu)$ and $\mathrm{Br}(Z' \to q_d\bar{q}_d)$ with respect to $\mathrm{Br}(Z' \to \ell^+\ell^-)$ and $\mathrm{Br}(Z' \to q_u\bar{q}_u)$.

Talking about all other decay channels, which actually define $\mathrm{Br}(Z' \to e^+e^-)$ and $\mathrm{Br}(Z'' \to e^+e^-)$, there are four more decays: $q\bar{q}$, $\nu\bar{\nu}$, VV, and Vh channels as one can see from Fig. 6 (as well as analogous Figs. 20 and 21 from the Appendix A 5 b), which are already mentioned above. Besides the dominant role of WW and ZH channels for large values of $\tilde{g}$, one should note dips in Z' and Z'' branchings into these channels occurring for small-intermediate values of $\tilde{g}$. This happens because the respective $Z'^{(\prime\prime)}WW$ and $Z'^{(\prime\prime)}ZH$ couplings change the sign around these dips, such that at the dips the respective branchings go to zero. The reason for this is the cancellation occurring because of the contribution from several different terms to these couplings—from gauge kinetic terms as well as from r_2 and r_3 terms from the Lagrangian defined by Eq. (5). One should note that in the case of such a cancellation and absence of ZH signal, which has been explored by the ATLAS Collaboration to probe WTC parameter space [22], the role of dilepton searches in probing WTC parameter space becomes especially appealing as a crucial complementary channel.

C. Cross sections

Both Z' and Z'' can be resonantly produced in a DY process, giving rise to dilepton signatures. The cross

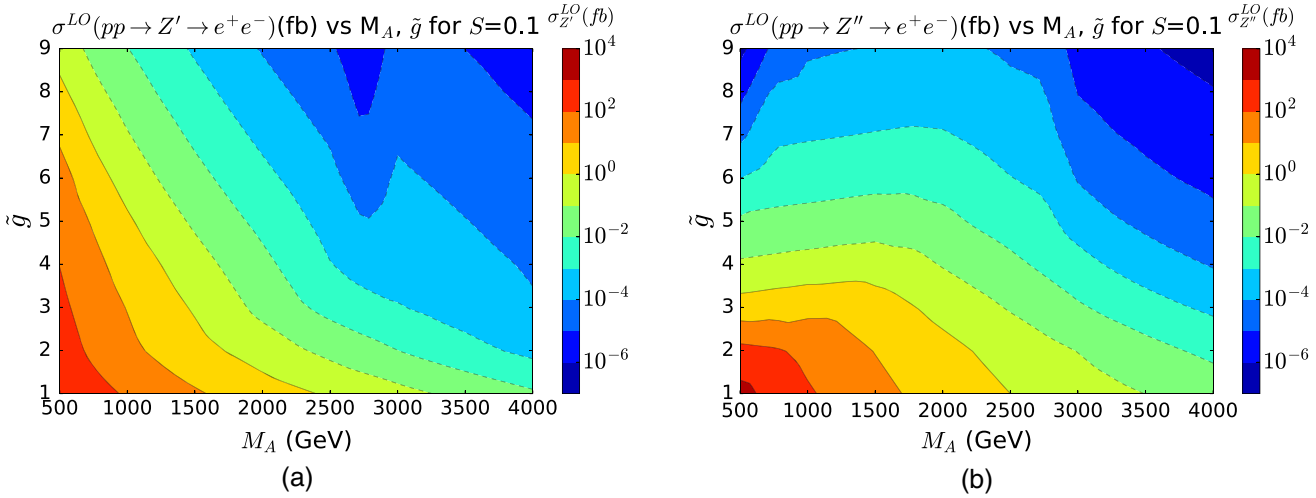

FIG. 8. (a) $\sigma^{\mathrm{LO}}(pp \to Z' \to e^+e^-)$ (fb) and (b) $\sigma^{\mathrm{LO}}(pp \to Z'' \to e^+e^-)$ (fb) at $\sqrt{s} = 13$ TeV as a function of M_A, $\tilde{g}$ at benchmark values of $S = 0.1$ and $s = 0$.

TABLE IV. Cross section $\sigma(pp \to Z'/Z'')$ at LO in the M_A, $\tilde{g}$, S parameter space at $\sqrt{s} = 13$ TeV, displayed in the format $\sigma_{Z'}$ ($\sigma_{Z''}$) in fb for each parameter space value.

		M_A [GeV]			
S	$\tilde{g}$	1000	1500	2000	2500
−0.1	1	$6.37 \times 10^2 (3.08 \times 10^3)$	$1.03 \times 10^2 (4.29 \times 10^2)$	23.7(83.5)	6.54(19.1)
	3	$3.37 \times 10^2 (2.39 \times 10^2)$	49.6(52.2)	10.4(14.1)	2.66(4.31)
	5	$1.43 \times 10^2 (37.1)$	22.9(9.83)	5.29(2.84)	1.47(0.89)
	7	80.2(7.89)	13.0(2.54)	3.03(0.81)	0.85(0.26)
	9	53.9(2.00)	8.78(0.74)	2.05(0.25)	$0.58(8.59 \times 10^{-2})$
0.1	1	$6.39 \times 10^2 (3.10 \times 10^3)$	$1.04 \times 10^2 (4.34 \times 10^2)$	24.0(84.7)	6.64(19.5)
	3	$3.06 \times 10^2 (2.72 \times 10^2)$	39.8(65.3)	5.79(20.0)	0.96(6.50)
	5	$1.17 \times 10^2 (47.7)$	18.5(14.4)	4.03(4.72)	0.81(1.89)
	7	54.0(11.5)	8.75(4.70)	2.01(1.85)	0.52(0.76)
	9	27.7(3.22)	4.50(1.73)	1.05(0.85)	0.29(0.41)
0.3	1	$6.43 \times 10^2 (3.12 \times 10^3)$	$1.05 \times 10^2 (4.40 \times 10^2)$	24.3(85.8)	6.75(19.8)
	3	$2.70 \times 10^2 (3.15 \times 10^2)$	16.1(93.9)	8.68(19.0)	3.47(4.70)
	5	90.4(63.2)	11.8(24.1)	6.98(3.82)	2.64(1.04)
	7	27.9(17.6)	4.30(10.2)	5.18(1.09)	2.64(0.31)
	9	1.35(5.65)	0.22(5.43)	$5.13(5.22 \times 10^{-2})$	$4.79(1.47 \times 10^{-2})$

section rates are directly related to Z' and Z'' coupling to fermions and dilepton branching ratios discussed earlier. Production cross sections for leading order (LO) DY $pp \to Z'/Z'' \to e^+e^-$ processes for LHC@13 TeV are presented in Fig. 8 as contour levels of the cross section in $(M_A, \tilde{g})$ space for $S = 0.1$ (see also Figs. 24 and 25 for analogous results for different values of S in the Appendix A 5 c) as well as in Table IV as numerical results for the 3D $(M_A, \tilde{g}, S)$ grid. Cross sections are calculated using CalcHEP [47] via the High Energy Physics Model Database (HEPMDB) [50], linked to the IRIDIS4 supercomputer. The parton density function (PDF) set used is NNPDF23 LO `as_0130_QED` [51], and the QCD scale Q is set to be the dilepton invariant mass, $Q = M(e^+e^-)$. The cross section has been evaluated in the narrow width approximation (NWA) to be consistent with the latest CMS limit [52], which we use for the interpretation of our signal as we discuss below. In the experimental CMS paper the cross section for Z' models was calculated in a mass window of $\pm 5\% \sqrt{s}$ at the resonance mass, following the prescription of Ref. [53] where it was checked that for this cut the cross section is close to the one from the NWA to within 10%. To account for next-to-next leading order (NNLO) QCD effects in our analysis below, the LO cross sections are multiplied by a mass-dependent K factor that was found using the ZWPROD program [54–56], which we have modified to evaluate the cross sections for Z' and W' resonances and linked to the LHAPDF6 library [57] as described in Ref. [58]. The resulting NNLO K factors are presented in Table V.

From Fig. 8 one can observe for Z' and Z'' DY cross sections an expected $1/\tilde{g}$ suppression discussed above as well as eventual PDF suppression with the increase of the mass of the resonances. Also, one should make an important remark that in the large mass region for low-intermediate values of $\tilde{g}$ the signal from the Z'' is higher than the one from the Z'. This highlights the complementarity between the two resonances, indicating that the Z' and Z'' DY processes will exclude different areas of the parameter space. This motivates our study of both resonances in conjunction, as we will exclude a greater portion of the parameter space with combined searches.

D. Z'/Z'' interference and validity of the reinterpretation of the LHC limits

Following our results in the previous section, we explore the interference between the Z' and Z'' boson, which gives rise to the dilepton signature. This is an important point for our study since we aim to reinterpret the LHC limits based on a *single* resonance search in the dilepton channel. Besides interference, the validity of such an interpretation also depends on how well these resonances are separated, their relative contribution to the signal, and their width-to-mass ratio. As discussed, for example, in [60], the interference effects between several resonances of the model can have a significant impact on the signal shape and can shift the peak away from the resonant mass. In such cases, one can no longer use the single resonance limit from LHC for the interpretation of the signal from individual Z' in the theory. Let us see if this is the case of the WTC model.

In Fig. 9(a) the contour levels for $pp \to Z' \to e^+e^-$ production cross section at the LHC@13 TeV as well as the relative ratio of dilepton rates for Z' vs Z'' production for $S = 0.1$ are shown. As in the recent experimental CMS paper, the cross section for Z' and Z'' was evaluated using finite width and mass window of $\pm 5\% \sqrt{s}$ at the resonance mass to correctly estimate the size of the Z'/Z''

TABLE V. K factors for NNLO QCD corrections to Drell-Yan cross sections at $\sqrt{s} = 13$ TeV evaluated with the help of the modified ZWPROD program as described in the text, using NNPDF23 LO `as_0130_QED` and NNPDF23 NNLO `as_0119_QED` [59] PDFs for LO and NNLO cross sections, respectively.

$M_{Z'}$ [GeV]	K_{NNLO}
500	1.35
600	1.36
700	1.36
800	1.37
900	1.38
1000	1.39
1100	1.39
1200	1.40
1300	1.40
1400	1.41
1500	1.41
1600	1.41
1700	1.42
1800	1.42
1900	1.42
2000	1.41
2100	1.41
2200	1.41
2300	1.41
2400	1.40
2500	1.40
2600	1.39
2700	1.39
2800	1.38
2900	1.37
3000	1.36
3100	1.35
3200	1.34
3300	1.33
3400	1.32
3500	1.31
3600	1.30
3700	1.29
3800	1.28
3900	1.26
4000	1.25
4100	1.24
4200	1.22
4300	1.21
4400	1.19

interference. Qualitatively the picture is similar for other values of the S parameter. First of all, one can notice that with an integrated luminosity of about 40 fb^{-1} (for which the limits on dilepton resonances are publicly available), one can expect a limit on the dilepton cross section of the order of 0.1 fb, which translates to M_A of about 3 TeV for low $\tilde{g}$ values. As we will see in the following section, this rough estimation agrees with an accurate limit we establish later in our paper. Second, one can clearly see that the role of Z'' becomes important and even dominant for M_A above 1.5 TeV and $\tilde{g}$ below about 4. Figure 9(b) presents the interference between Z' and Z'' contributing to the dilepton signature. One can see that the interference is at the percent level and can be safely neglected. This is an important condition for interpretation of the LHC limits on a single resonance search that was the subject of phenomenological and experimental studies for decades, for a review see Refs. [49,61,62] and references therein. Taking this into account as well as the fact that the Z' contribution to the dilepton signature is dominant, in the region of small $M_A < 1$ TeV we conclude that one can use LHC limits for dilepton single resonance searches. Using similar logic, one can see that in the region of intermediate and large $M_A > 1.5$ TeV where the $M_{Z''}$ contribution to the dilepton signature is dominant, one can use LHC limits for single resonance dilepton searches in the case of Z''.

Finally, in the intermediate region of M_A between 1 and 1.5 TeV when dilepton signals from Z' and Z'' are comparable, well separated in mass (above 10%) recalling $Z' - Z''$ mass difference from Fig. 2 and their width-to-mass ratio is small (few percent) (Fig. 5), the LHC limits can be applied *separately* to Z' or Z'' signatures. Therefore in the whole parameter space of interest [with $\sigma(pp \to Z'/Z'' \to \ell^+\ell^-) \simeq 0.1$ fb] one can use the signal either from Z' or Z'' to best probe the model parameter space. This procedure sets the strategy that we use in the following section. The statistical combination of signatures from both resonances is outside of the scope of this paper since it requires also the change to the procedure in setting the limit at the experimental level.

E. Probing technicolor parameter space at the LHC

1. The setup for the LHC limits

The CMS Z' dielectron 13 TeV limits [52] that we use for the interpretation of the WTC parameter space are expressed as $R_\sigma = \sigma(pp \to Z' \to e^+e^-)/\sigma(pp \to Z \to e^+e^-)$, which is the ratio of the cross section for dielectron production through a Z' boson to the cross section for dielectron production through a Z boson. The limits are expressed as a ratio in order to remove the dependency on the theoretical prediction of the Z boson cross section and correlated experimental uncertainties.

To reproduce these limits, a simulated dataset of the CMS mass distribution is generated using a background probability density function:

$$m^\kappa e^{\alpha+\beta m+\gamma m^2+\delta m^3+\epsilon m^4}, \tag{28}$$

where κ, α, β, γ, δ and ϵ are function parameters. This probability density function was used to describe the dielectron mass background distribution, where the background is predominantly Drell-Yan dielectron events. A simulated CMS dataset is obtained by normalizing the Z

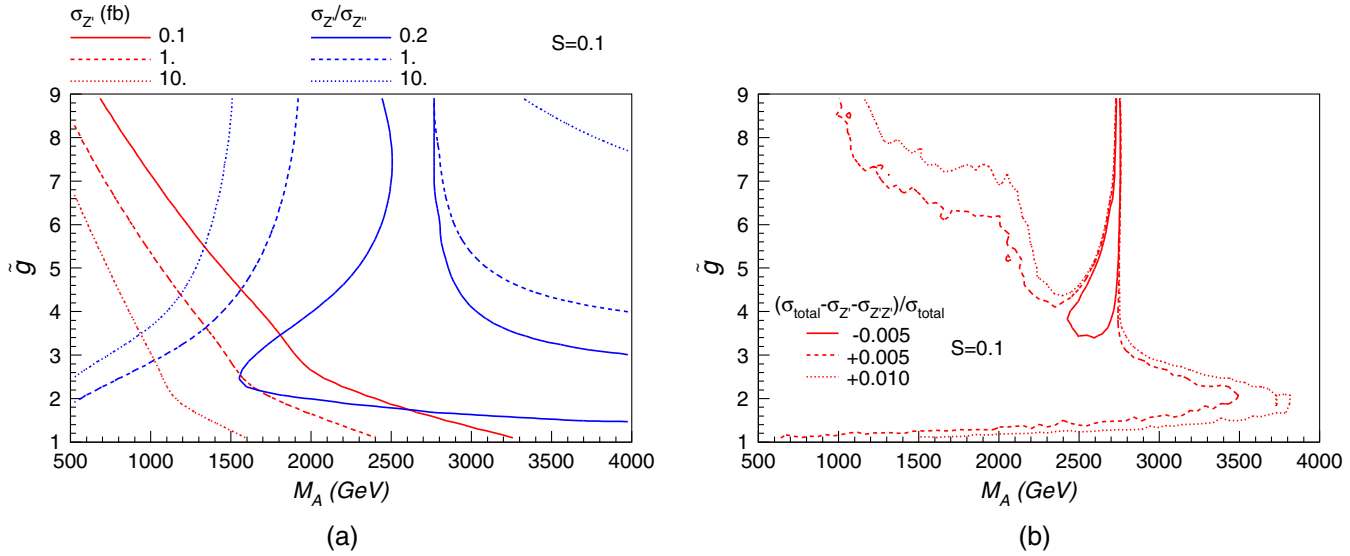

FIG. 9. (a) The contour levels for $pp \to Z' \to e^+e^-$ production cross section at the LHC@13 TeV as well as the relative ratio of dilepton rates for Z' vs Z'' production for $S = 0.1$. (b) The interference between Z' and Z'' contributing to the dilepton signature from $pp \to Z'/Z'' \to \ell^+\ell^-$ process.

boson region ($60 < m_{ee} < 120$ GeV) in simulation to data. The total number of data events corresponding to a given integrated luminosity is N_{Lumi}. Using the above probability density function we generate hundreds of datasets, each with a total number of events that is a Poisson fluctuation on N_{Lumi}. For each dataset we step through mass values and set a 95% confidence level (C.L.) limit on R_σ. The limits are set using a Bayesian method with an unbinned extended likelihood function. Using both the signal and background probability density functions, the likelihood distribution is calculated as a function of the number of signal events for a given mass. The 95% C.L. upper limit on the number of signal events N_{95} for a given mass is taken to be the value such that integrating the likelihood from 0 to N_{95} is 0.95 of the total likelihood integral. This number N_{95} is converted to a limit on the ratio of cross sections by dividing by the total number of acceptance and efficiency corrected Z bosons, the signal acceptance, and the efficiency. At each mass point, a limit is calculated for each of the hundreds of simulated datasets. Using the limits computed from each simulated dataset, the median 95% C.L. limit and the one and two sigma standard deviations on the 95% C.L. limit for each mass point can be calculated. The signal probability distribution used in the likelihood is a convolution of a Breit-Wigner function and a Gaussian function with exponential tails to either side. The limits are calculated in a mass window of ± 6 times the signal width, with this window being symmetrically enlarged until there is a minimum of 100 events in it.

To generate 14 TeV dataset limits, the above procedure is repeated but the background probability density function is multiplied by an NNPDF scale factor to convert the 13 TeV background distribution into a 14 TeV distribution. In this work the PDF set NNPDF LO `as_0130_QED` is applied.

2. LHC potential to probe walking technicolor parameter space

With the setup described above we have evaluated limits on the NMWT parameter space according to Run 2 at CMS. We use the 95% C.L. observed limit on $\sigma(pp \to Z' \to e^+e^-)/\sigma(pp \to Z \to e^+e^-)$ at $\sqrt{s} = 13$ TeV based on a dataset of integrated luminosity 36 fb^{-1} [52]. A similar limit is also obtained by the ATLAS Collaboration in Ref. [63].

The SM DY cross section at NNLO is given to be $\sigma(pp \to Z/\gamma^* \to e^+e^-) = 1.928$ nb, which we use to convert the ratio of cross sections to a limit on $\sigma(pp \to Z' \to e^+e^-)$. This limit is then projected onto the $(M_A, \tilde{g})$ plane and compared to the signal cross sections for Z' and Z'' which we have evaluated at NNLO level. Figure 10(a) presents the NMWT parameter space in the $(M_A, \tilde{g})$ plane for $S = 0.1$ which is already excluded with the recent CMS results. One can observe an important complementarity of Z' and Z''; as was expected from the plots with cross sections, Z'' extends the coverage of the LHC in the large $\tilde{g}$ and M_A region. Analogous exclusion plots for different values of S are presented in Figs. 26(a), 27(a), 28(a) and 29(a) for $S = -0.1$, 0.0, 0.2, and 0.3, respectively.

We have also found the projected LHC limit for higher integrated luminosities. To do this we have simulated the SM DY background and have obtained an expected limit for 36 fb^{-1}, confirming to within a few % the CMS expected limits using the method described in the previous

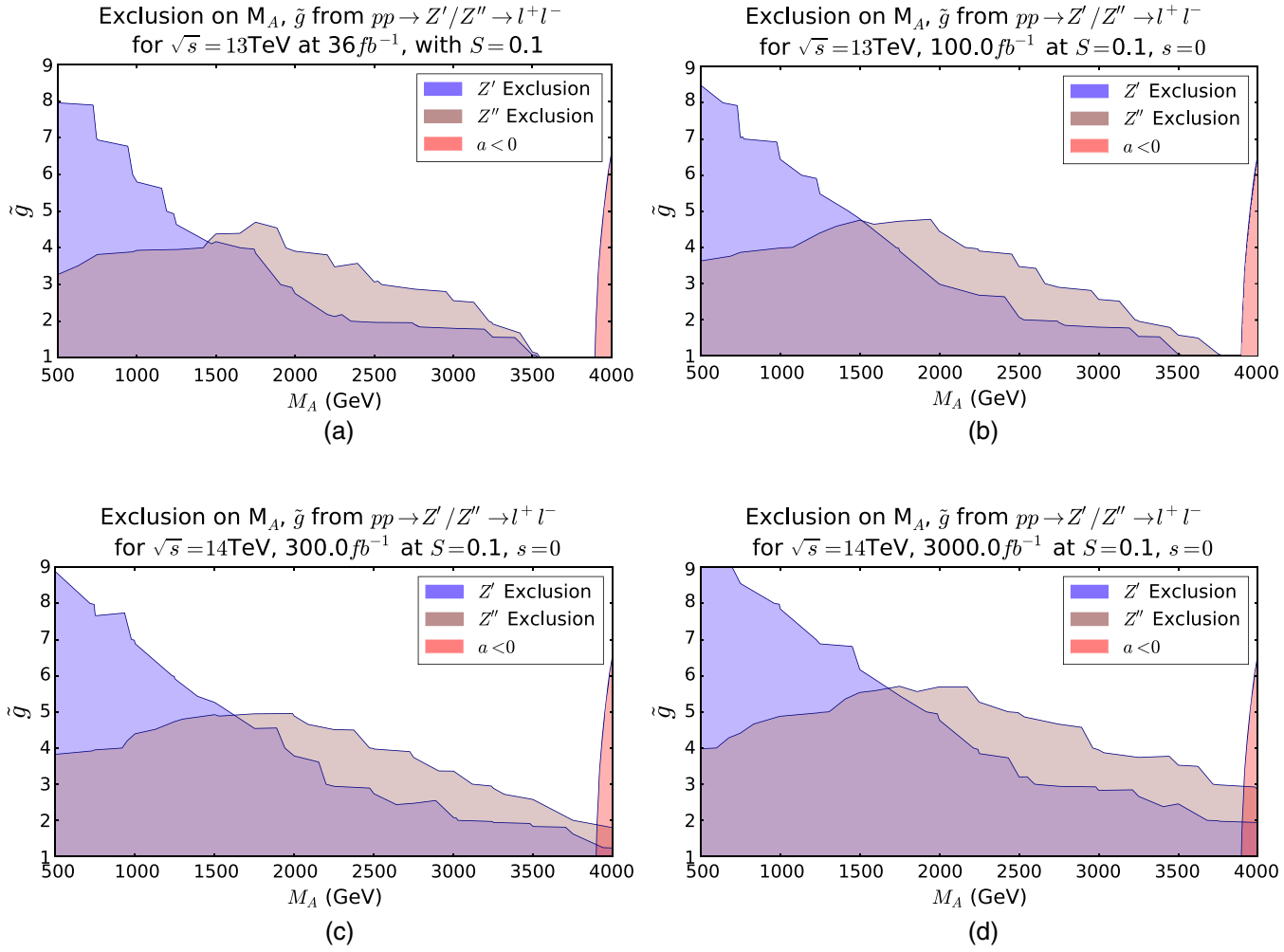

FIG. 10. Exclusion of the M_A-$\tilde{g}$ parameter space from Z' and Z'' DY processes at $\sqrt{s} = 13$ TeV and luminosity of 36 fb^{-1} (a). Predicted exclusion regions for the NMWT parameter space at (a) $\sqrt{s} = 13$ TeV and $\mathcal{L} = 100$ fb^{-1}, (b) $\sqrt{s} = 14$ TeV and $\mathcal{L} = 300$ fb^{-1}, and (c) $\sqrt{s} = 14$ TeV and $\mathcal{L} = 3000$ fb^{-1}.

section for the sake of its validation. Then we have obtained analogous expected limits for 100 fb^{-1} at $\sqrt{s} = 13$ TeV as well as for 300 fb^{-1} and 3000 fb^{-1} at $\sqrt{s} = 14$ TeV. We follow the CMS limit setting procedure except for mass points with less than 10 events where we set limits using Poisson statistics. The excluded regions of the M_A, $\tilde{g}$ parameter space are shown in Figs. 10(b), 10(c), and 10(d), respectively. Analogous exclusion plots for different values of S are presented in Figs. 26–29 for $S = -0.1$, 0.0, 0.2, and 0.3, respectively.

Already at 100 fb^{-1} the excluded region visibly increases in M_A and $\tilde{g}$ for both Z' and Z'' resonances. For example, for small values of $\tilde{g}$ it increases for M_A from 3.5 TeV to about 3.8 TeV. Figure 10 also shows the theoretical upper limit on M_A imposed by the a parameter (see Sec. II). Requiring $a > 0$ and combining it with the current or projected experimental limits, one gets the full picture of the surviving parameter space.

With the beam energy increase to $\sqrt{s} = 14$ TeV and total integrated luminosity 300 fb^{-1} or more the entire range of M_A that we explore is excluded in the region of $\tilde{g} < 2$, and the predictions for the final high-luminosity run of the LHC [Fig. 10(d)] increase the exclusions in both the M_A and $\tilde{g}$ directions ruling out the whole parameter space for $\tilde{g} < 3$.

To see the picture of the LHC sensitivity to the *whole* NMWT parameter space we have performed a scan of the full 4D (M_A, $\tilde{g}, S, s$) parameter space with $\sim 1 \times 10^7$ random points. In Fig. 11 we present the projection of this scan into the (M_A, $\tilde{g}$) plane, with S and s ranges $(-0.1, 0.3)$ and $(-1, 1)$, respectively, for LHC@13 TeV and 36 fb^{-1} integrated luminosity. In Fig. 11(a) we overlaid the excluded points from Z' or Z'' signals on top of the allowed points to show the $(M_A, \tilde{g})$ parameter space, which is allowed for all values of S and s parameters, while in Fig. 11(b) we overlaid the allowed points on top of the

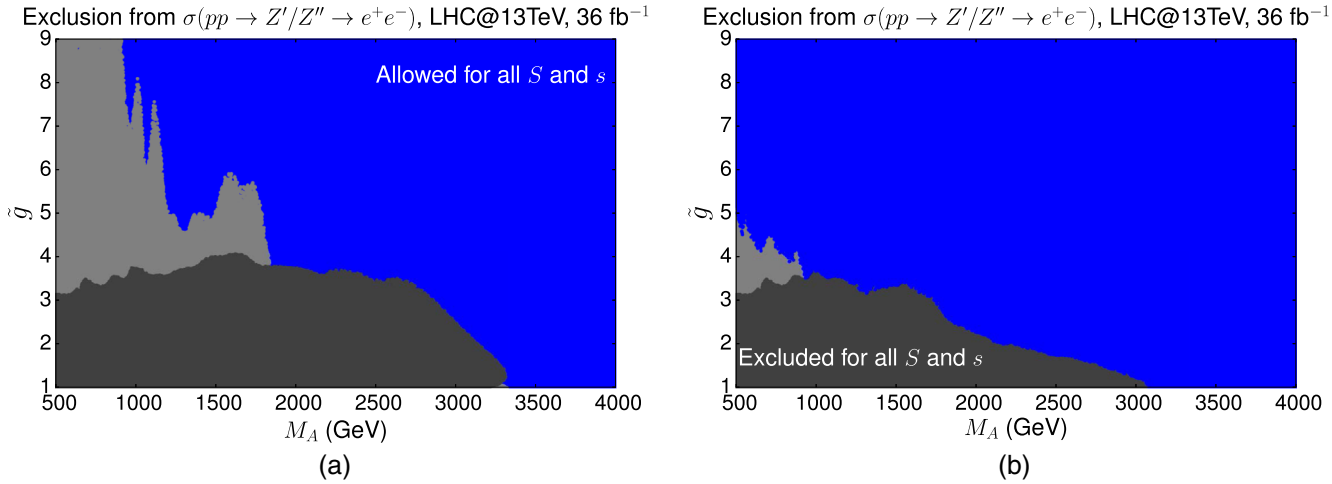

FIG. 11. Projections on M_A, $\tilde{g}$ parameter space of theoretical DY Z'/Z'' cross section showing the allowed for all S and s region (a), excluded for all S and s region (b) for the current CMS exclusion for LHC@13 TeV and 36 fb^{-1} integrated luminosity. Blue points are allowed, light grey points are excluded by the Z', and dark grey points are excluded by the Z''.

excluded points to show the $(M_A, \tilde{g})$ parameter space, which is excluded for all values of S and s parameters. The excluded points from the Z'' cross section (dark grey) are layered on top of those excluded by the Z' cross section (light grey). It is important to stress that the most conservative limit on M_A (parameter space that is excluded for all values of S and s parameters) is about 3.1 TeV for low values of $\tilde{g}$ and that this limit is significantly higher (by about 1 TeV) than previous limits established by the ATLAS Collaboration in Refs. [21,22] for $S = 0.3$, $s = 0$ benchmark in the $(M_A, \tilde{g}, S, s)$ plane, which actually gives one of the most optimistic limits for NMWT.

IV. CONCLUSIONS

Walking technicolor remains one of the most appealing BSM theories involving strong dynamics. In this study we have fully explored the 4D parameter space of WTC using dilepton signatures from Z'/Z'' production and decay at the LHC. This signature is the most promising one for discovery of WTC at the LHC for the low-intermediate values of the $\tilde{g}$ parameter.

We have studied the complementarity of the dilepton signals from both heavy neutral vector resonances and have demonstrated its importance. As a result, we have established the most up-to-date limit on the WTC parameter space and provided projections for the LHC potential to probe WTC parameter space at a higher future luminosity and upgraded energy.

Our results on the LHC potential to probe WTC parameter space are presented in Figs. 26, 27, 10, 28, and 29 for the $(M_A, \tilde{g})$ plane for $S = -0.1, 0.0, 0.1, 0.2$, and 0.3, respectively, which gives a clear idea how the properties of the model and the respective LHC reach depend on the value of the S parameter. This extends the results found previously for just $S = 0.3$, which is not quite motivated in light of the present EWPD. Moreover, as another new element of the exploration of WTC, we have provided an analytic description for features such as the Z'/Z'' masses, the mass inversion M_{inv} point, as well as some couplings in our paper. We have also presented all these properties in the form of figures in the $(M_A, \tilde{g})$ plane and 3D $(M_A, \tilde{g}, S)$ tables for clear insight into the model behavior, and for direct comparison with prior works. We have discussed the theoretical upper limit on M_A from the requirement of "walking" dynamics, and in combination with the exclusions from experiment we have found the strongest constraints on WTC to date. The predicted exclusions indicate that within the scope of the LHC, the low $\tilde{g}$ regions of the WTC parameter space can be closed completely.

We have explored the effect of the S and s parameters on the WTC exclusions using a very detailed scan of the 4D parameter space and establishing the current LHC limit in this 4D space which we present in Fig. 11. The results we have found reflect the most conservative limit on M_A around 3.1 TeV, which for low values of $\tilde{g}$ is significantly higher (by about 1 TeV) than previous limits established by the ATLAS Collaboration in Refs. [21,22] for the most optimistic benchmark with $S = 0.3$. The complete 4D scan also indicates the important influence of the value of the S parameter on the dilepton signal rate, while the s parameter has little effect on the rate of the dilepton signal but could be important for the complementary VV and VH signatures.

Besides the Z' and Z'' complementarity for the exploration of the dilepton signal in the low to intermediate $\tilde{g}$ region, it is important to note the further complementarity of the VV and VH signatures that would allow us to probe the large values of $\tilde{g}$ up to $\tilde{g} \lesssim 10$. Beyond this value, the ratios $\Gamma_{Z',Z''}/M_{Z',Z''}$ will (with some dependence on the

values of S and M_A) grow beyond unity as seen in Fig. 5. Here the effective Lagrangian used is no longer valid. Conversely the success of vector meson dominance in QCD indicates that the effective Lagrangian is a good description up to these values of $\tilde{g}$. The VV and VH signatures are the subject of the upcoming study [64].

ACKNOWLEDGMENTS

The authors acknowledge the use of the IRIDIS High Performance Computing Facility, and associated support services at the University of Southampton, in the completion of this work. A. B. acknowledges partial support from the STFC Grant No. ST/L000296/1. A. B. also thanks the NExT Institute, Royal Society Leverhulme Trust Senior Research Fellowship LT140094, Royal Society International Exchange Grant No. IE150682 and Soton-FAPESP grant. A. B. acknowledges partial support from the InvisiblesPlus RISE from the European Union Horizon 2020 research and innovation program under the Marie Sklodowska-Curie Grant Agreement No. 690575. A. C. acknowledges the University of Southampton for support under the Mayflower Scholarship Ph.D. program. A. C. acknowledges partial support from SEPnet under the GRADnet Scholarship award.

APPENDIX A

1. Mass matrices in NMWT

We calculate N_{ij} by diagonalizing the bosonic mixing matrices Eq. (A3), perturbatively calculating the eigenvalues and eigenvectors of the matrices that diagonalize $\mathcal{M}_C^2$ and $\mathcal{M}_N^2$ order by order in $1/\tilde{g}$. Details of the calculation are presented here, with the results for C_{ij} and N_{ij} to second order in $1/\tilde{g}$.[2] At zeroth order, the eigenvalues for the γ, Z are degenerate and m_γ^2, $m_Z^2 = 0$, so the eigenvectors cannot be uniquely defined at this stage. To resolve this degeneracy we introduce a generic parameter x that is fixed at second order to be $x = g_2/g_1$.

From the covariant derivative terms of the effective bosonic Lagrangian equation (5), we construct the mixing matrices that diagonalize to give physical masses for the vector bosons. The Lagrangian of the vector bosons in the mass eigenbasis is

$$\mathcal{L}_{\text{mass}} = (\,\tilde{W}_\mu^- \quad A_{L\mu}^- \quad A_{R\mu}^-\,)\mathcal{M}_C^2 \begin{pmatrix} \tilde{W}^{+\mu} \\ A_L^{+\mu} \\ A_R^{+\mu} \end{pmatrix} + \frac{1}{2}(\,\tilde{B}_\mu \quad \tilde{W}_\mu^0 \quad A_{L\mu}^0 \quad A_{R\mu}^0\,)\mathcal{M}_N^2 \begin{pmatrix} \tilde{B}^\mu \\ \tilde{W}^{0\mu} \\ A_L^{0\mu} \\ A_R^{0\mu} \end{pmatrix}, \tag{A1}$$

where these mass matrices for the charged and neutral bosons are

$$\mathcal{M}_C^2 = \begin{pmatrix} \frac{g_2^2}{\tilde{g}^2}M_V^2(1+\omega) & -\frac{g_2}{\sqrt{2}\tilde{g}}M_A^2\chi & -\frac{g_2}{\sqrt{2}\tilde{g}}M_V^2 \\ -\frac{g_2}{\sqrt{2}\tilde{g}}M_A^2\chi & M_A^2 & 0 \\ -\frac{g_2}{\sqrt{2}\tilde{g}}M_V^2 & 0 & M_V^2 \end{pmatrix}, \tag{A2}$$

$$\mathcal{M}_N^2 = \begin{pmatrix} \frac{g_1^2}{\tilde{g}^2}M_V^2(1+\omega) & -\frac{g_1 g_2}{\tilde{g}^2}M_V^2\omega & \frac{g_1}{\sqrt{2}\tilde{g}}M_A^2\chi & -\frac{g_1}{\sqrt{2}\tilde{g}}M_V^2 \\ -\frac{g_1 g_2}{\tilde{g}^2}M_V^2\omega & \frac{g_2^2}{\tilde{g}^2}M_V^2(1+\omega) & -\frac{g_2}{\sqrt{2}\tilde{g}}M_A^2\chi & -\frac{g_2}{\sqrt{2}\tilde{g}}M_V^2 \\ \frac{g_1}{\sqrt{2}\tilde{g}}M_A^2\chi & -\frac{g_2}{\sqrt{2}\tilde{g}}M_A^2\chi & M_A^2 & 0 \\ -\frac{g_1}{\sqrt{2}\tilde{g}}M_V^2 & -\frac{g_2}{\sqrt{2}\tilde{g}}M_V^2 & 0 & M_V^2 \end{pmatrix}. \tag{A3}$$

In order to perform the analytic diagonalization of these matrices, we perform an expansion in $1/\tilde{g}$ and calculate the eigenvectors and eigenvalues of the matrix order by order. Rephrasing the χ and M_V^2 parameters such that

$$M_V^2 = \frac{F_\pi^2\tilde{g}^2}{2} + M_A^2\chi^2, \qquad \chi = \sqrt{1 - \frac{S\tilde{g}^2}{8\pi}},$$

we can rewrite these matrices in terms of the parameters of the model that we have used in this paper. Furthermore, from the WSRs [43] we set $\omega = 0$ and fix $F_\pi = 246$ GeV, so the mass matrices are written entirely from the free parameters, M_A, $\tilde{g}$, and S.

[2]Each of these C_{ij} and N_{ij} represent the mixing of the vector boson/meson states; e.g., N_{24} represents a mixed $Z - Z''$ state, and components with $i = j$ represent the mixing of a gauge field with itself.

Consider the diagonalization of the neutral matrix $\mathcal{M}_N^2$, Eq. (A3). From the logic above we see that this can be written as

$$\mathcal{M}_N^2 = \begin{pmatrix} \frac{1}{8}g_1^2\left(M_A^2\left(\frac{8}{\tilde{g}^2}-\frac{S}{\pi}\right)+4F_\pi^2\right) & 0 & \frac{g_1 M_A^2}{4\tilde{g}}\sqrt{8-\frac{\tilde{g}^2 S}{\pi}} & \frac{g_1}{8\pi\sqrt{2}\tilde{g}}(M_A^2(\tilde{g}^2 S-8\pi)-4\tilde{g}^2\pi F_\pi^2) \\ 0 & \frac{1}{8}g_2^2(M_A^2(\frac{8}{\tilde{g}^2}-\frac{S}{\pi})+4F_\pi^2) & -\frac{g_2 M_A^2}{4\tilde{g}}\sqrt{8-\frac{\tilde{g}^2 S}{\pi}} & \frac{g_2}{8\pi\sqrt{2}\tilde{g}}(M_A^2(\tilde{g}^2 S-8\pi)-4\tilde{g}^2\pi F_\pi^2) \\ \frac{g_1}{8\pi\sqrt{2}\tilde{g}}(M_A^2(\tilde{g}^2 S-8\pi)-4\tilde{g}^2\pi F_\pi^2) & -\frac{g_2 M_A^2}{4\tilde{g}}\sqrt{8-\frac{\tilde{g}^2 S}{\pi}} & M_A^2 & 0 \\ \frac{g_1}{8\pi\sqrt{2}\tilde{g}}(M_A^2(\tilde{g}^2 S-8\pi)-4\tilde{g}^2\pi F_\pi^2) & \frac{g_2}{8\pi\sqrt{2}\tilde{g}}(M_A^2(\tilde{g}^2 S-8\pi)-4\tilde{g}^2\pi F_\pi^2) & 0 & M_A^2(1-\frac{\tilde{g}^2 S}{8\pi})+\frac{1}{2}\tilde{g}^2 F_\pi^2 \end{pmatrix}. \tag{A4}$$

To expand in powers of $1/\tilde{g}$ we can rewrite the independent M_A, S, and F_π parameters in terms of $\tilde{g}$ and dependent parameters of the model. As stated above, in the regime of large $\tilde{g}$, M_A^2 is dominated by the r_2 term of Eq. (6); however, it is not obvious to see that in the case of small $\tilde{g}$, the m^2 term dominates. We can determine the scaling of m^2 from the first WSR and the definition of the pion decay constant in NMWT. From Eq. (8) we see that F_π^2 can be written in terms of $M_A^2/\tilde{g}^2$. In the low $\tilde{g}$ regime this would lead to $F_\pi^2 \propto m^2/\tilde{g}^2$, so one would naïvely expect $F_\pi \propto 1/\tilde{g}$. However, F_π is fixed to avoid deviations from the first WSR, so m^2 *must* itself scale with $\tilde{g}^2$. Finally, from Eq. (17) we see that S can be written in terms of $\tilde{g}^{-2}$.

At leading order in $1/\tilde{g}$, the mass squared terms for the neutral bosons are

$$M_\gamma^2 = 0, \qquad M_Z^2 = 0, \qquad M_{Z'}^2 = M_A^2,$$
$$M_{Z''}^2 = M_A^2\left(1-\frac{\tilde{g}^2 S}{8\pi}\right)+\frac{1}{2}\tilde{g}^2 F_\pi^2. \tag{A5}$$

As there are two degenerate eigenvalues $= 0$, we must define the eigenvectors at zeroth order with a generic term x which is fixed only at second order in the $1/\tilde{g}$ expansion. The zeroth order eigenvectors are then

$$\bar{v}_0 = \begin{pmatrix} \frac{x}{\sqrt{1+x^2}} & \frac{1}{\sqrt{1+x^2}} & 0 & 0 \\ \frac{1}{\sqrt{1+x^2}} & -\frac{x}{\sqrt{1+x^2}} & 0 & 0 \\ 0 & 0 & 1 & 0 \\ 0 & 0 & 0 & 1 \end{pmatrix}. \tag{A6}$$

We can now construct the higher order corrections order by order. To calculate the first order corrections, we consider the eigenvalue equation

$$M\bar{v} = \lambda\bar{v}, \tag{A7}$$

where $M = M_0 + M_1 + M_2 + \cdots$ is the mixing matrix, $\bar{v} = \bar{v}_0 + \bar{v}_1 + \bar{v}_2 + \cdots$ are the eigenvectors of M, and $\lambda = \lambda_0 + \lambda_1 + \lambda_2 + \cdots$ are the eigenvalues of M. At first order we have

$$\begin{aligned} (M_0+M_1)(\bar{v}_0+\bar{v}_1) &= (\lambda_0+\lambda_1)(\bar{v}_0+\bar{v}_1), \\ M_0\bar{v}_1 + M_1\bar{v}_0 + M_1\bar{v}_1 &= \lambda_0\bar{v}_1 + \lambda_1\bar{v}_0 + \lambda_1\bar{v}_1, \\ \lambda_1 &= \bar{v}_0^T(M_0-\lambda_0)\bar{v} + \bar{v}_0^T M_1\bar{v}_0, \\ \lambda_1 &= \bar{v}_0^T M_1\bar{v}_0, \end{aligned}$$

where we have used the zeroth order eigenvalue equation $M_0\bar{v}_0 = \lambda_0\bar{v}_0$ to remove zeroth order terms and have discarded terms of order > 1.

We can immediately see that the first order eigenvalues are $\lambda_1^i = 0$ for all $i = 1, \ldots, 4$, as $\mathcal{M}_N^2$ does not have any diagonal components at order $1/\tilde{g}$. We do not expect to see corrections to the squared masses of the vector bosons at odd order in $1/\tilde{g}$ as then we would find mass terms dependent on fractional powers in the coupling. The eigenvectors will contribute to the second order mass corrections, and in terms of model parameters and the unknown x we find

$$\bar{v}_1 = \begin{pmatrix} 0 & 0 & \frac{g_2-g_1 x}{4\tilde{g}\sqrt{1+x^2}}\sqrt{8-\frac{\tilde{g}^2 S}{\pi}} & \frac{g_2+g_1 x}{\tilde{g}\sqrt{2}\sqrt{1+x^2}} \\ 0 & 0 & -\frac{g_1+g_2 x}{4\tilde{g}\sqrt{1+x^2}}\sqrt{8-\frac{\tilde{g}^2 S}{\pi}} & \frac{g_1-g_2 x}{\tilde{g}\sqrt{2}\sqrt{1+x^2}} \\ \frac{g_1}{4\tilde{g}}\sqrt{8-\frac{\tilde{g}^2 S}{\pi}} & -\frac{g_2}{4\tilde{g}}\sqrt{8-\frac{\tilde{g}^2 S}{\pi}} & 0 & 0 \\ -\frac{g_1}{\sqrt{2}\tilde{g}} & -\frac{g_2}{\sqrt{2}\tilde{g}} & 0 & 0 \end{pmatrix}. \tag{A8}$$

To find the second order eigenvalues, we follow the same procedure as above, and keeping only second order terms we find

$$\lambda_2 = \bar{v}_0^T M_1 \bar{v}_1 + \bar{v}_0^T M_2 \bar{v}_0 - \bar{v}_0^T \lambda_1 \bar{v}_1, \tag{A9}$$

where we use the fact that $\lambda_1 = 0$ to reduce this to

$$\lambda_2 = \bar{v}_0^T M_1 \bar{v}_1 + \bar{v}_0^T M_2 \bar{v}_0. \tag{A10}$$

At this order we can now fix x, which turns out to be $x = g_2/g_1$, and we arrive at the second order corrections to the neutral vector boson masses:

$$M_\gamma^2 = 0, \qquad M_Z^2 = \frac{1}{4}(g_1^2 + g_2^2)F_\pi^2, \tag{A11}$$

$$M_{Z'}^2 = \frac{g_1^2 + g_2^2}{16\pi\tilde{g}^2} M_A^2 (8\pi - \tilde{g}^2 S), \qquad M_{Z''}^2 = \frac{g_1^2 + g_2^2 + 2\tilde{g}^2}{16\pi\tilde{g}^2} (M_A^2(8\pi - \tilde{g}^2 S) + 4\pi\tilde{g}^2 F_\pi^2). \tag{A12}$$

Finally, the rotation matrices $\mathcal{C}$ and $\mathcal{N}$ can be constructed from the transpose of the sum of zeroth, first, and second order eigenvectors:

$$\mathcal{N} = \begin{pmatrix} \frac{g_2}{\sqrt{g_1^2+g_2^2}} & \frac{g_1}{\sqrt{g_1^2+g_2^2}} & \frac{g_1\chi}{\sqrt{2}\tilde{g}} & -\frac{g_1}{\sqrt{2}\tilde{g}} \\ \frac{g_1}{\sqrt{g_1^2+g_2^2}} & -\frac{g_2}{\sqrt{g_1^2+g_2^2}} & -\frac{g_2\chi}{\sqrt{2}\tilde{g}} & -\frac{g_2}{\sqrt{2}\tilde{g}} \\ 0 & -\frac{\sqrt{g_1^2+g_2^2}\chi}{\sqrt{2}\tilde{g}} & 1 & -\frac{(g_1-g_2)(g_1+g_2)(2M_A^2\chi^2+\tilde{g}^2F_\pi^2)\chi}{\tilde{g}^2M_A^2(4\chi^2-1)+2\tilde{g}^4F_\pi^2} \\ \frac{\sqrt{2}g_1g_2}{\sqrt{g_1^2+g_2^2}\tilde{g}} & \frac{(g_1-g_2)(g_1+g_2)}{\sqrt{2}\tilde{g}\sqrt{g_1^2+g_2^2}} & \frac{4(g_1-g_2)(g_1+g_2)M_A^2\chi}{2\tilde{g}^2M_A^2(\chi^2-4)+\tilde{g}^4F_\pi^2} & 1 \end{pmatrix}, \tag{A13}$$

$$\mathcal{C} = \begin{pmatrix} 1 & -\frac{g_2\chi}{\sqrt{2}\tilde{g}} & -\frac{g_2}{\sqrt{2}\tilde{g}} \\ \frac{g_2\chi}{\sqrt{2}\tilde{g}} & 1 & \frac{g_2\chi}{\sqrt{2}\tilde{g}}\left(1 + \frac{2M_A^2}{2M_A^2(3\chi^2-1)+3\tilde{g}^2F_\pi^2}\right) \\ \frac{g_2}{\sqrt{2}\tilde{g}} & -\frac{3g_2^2M_A^2\chi}{2\tilde{g}^2M_A^2(\chi^2-3)+\tilde{g}^4F_\pi^2} & 1 \end{pmatrix}, \tag{A14}$$

where $\mathcal{N}$ and $\mathcal{C}$ diagonalize the neutral and charged mass matrices, respectively. It is the elements of these rotation matrices that comprise the vector boson couplings in NMWT, as discussed in Sec. III A 2.

2. Dependent parameters in terms of S, M_A, $\tilde{g}$, s

From the equations defined in Sec. II, we derive expressions for all of the dependent parameters of NMWT in terms of its four independent parameters. Begin by constructing simultaneous equations for v and r_2 parameters, the first of which comes from rearranging Eq. (7),

$$v^2(r_2 + 1) = \frac{4M_A^2}{\tilde{g}^2}(1 - \chi), \tag{A15}$$

and the second from Eq. (6),

$$M_V^2 - M_A^2 = m^2 - m^2 + \frac{\tilde{g}^2(s - r_2)v^2}{4} - \frac{\tilde{g}^2(s + r_2)v^2}{4}, \tag{A16}$$

$$r_2 v^2 = \frac{2}{\tilde{g}^2}(M_A^2 - M_V^2). \tag{A17}$$

Then we resolve v by subtracting Eq. (A17) from Eq. (A15), and substituting the definitions of χ and M_V from Eqs. (18) and (A15), respectively,

$$v^2 = \frac{1}{\sqrt{2}G_F} + \frac{4M_A^2}{\tilde{g}^2}\left(1 - \frac{\tilde{g}^2 S}{16\pi} - \sqrt{1 - \frac{\tilde{g}^2 S}{8\pi}}\right). \tag{A18}$$

Then we substitute this into Eq. (A17) to find r_2,

$$r_2 = \frac{\tilde{g}^2(G_F M_A^2 S - 2\sqrt{2}\pi)}{\tilde{g}^2(2\sqrt{2}\pi - G_F M_A^2 S) - 4G_F M_A^2(\sqrt{2\pi}\sqrt{8\pi - \tilde{g}^2 S} - 4\pi)}. \tag{A19}$$

Now we find m in terms of the NMWT parameters from Eq. (6),

$$m^2 = M_A^2 - \frac{\tilde{g}^2(s + r_2)v^2}{4}, \tag{A20}$$

$$m^2 = \frac{\tilde{g}^2(1-s)(2\sqrt{2}\pi - G_F M_A^2 S) + 4G_F M_A^2(4\pi(1-s) + s\sqrt{2\pi}\sqrt{8\pi - \tilde{g}^2 S})}{16\pi G_F}. \tag{A21}$$

Then we relate the Fermi constant G_F to the model parameters by finding the form of F_π. We combine the definitions of F_V and F_A with the first WSR,

$$F_\pi^2 = \frac{2M_V^2}{\tilde{g}^2} - \frac{2M_A^2}{\tilde{g}^2}\chi^2, \tag{A22}$$

and substitute the definition of χ from Eq. (7),

$$F_\pi^2 = \frac{2}{\tilde{g}}\left(\frac{v^2\tilde{g}^2 r_3}{2} - \frac{v^4\tilde{g}^4 r_3^2}{16M_A^2} - (r_3 - 1)\frac{v^2\tilde{g}^2}{2}\right). \tag{A23}$$

Finally, we arrive at the expression for F_π,

$$F_\pi^2 = v^2\left(1 - \frac{v^2\tilde{g}^2 r_3^2}{8M_A^2}\right). \tag{A24}$$

3. Solving for EW couplings

The other important quantities to derive analytic formulas for are the EW equivalent couplings g_1 and g_2 in terms of the independent parameters. These couplings can be derived as roots of the characteristic equation for the Z boson eigenvalue; i.e., we can solve the equation $\det[\mathcal{M}_N^2 - M_Z^2] = 0$. Taking the absolute values of the roots, we find two solutions to this equation that correspond to the couplings g_2 and g_1, respectively,

$$g2 = \tilde{g}\sqrt{\frac{(\tilde{g}^2 - 2e^2)abM_Z^2 + \sqrt{abM_Z^2(2e^2M_Z^2 + \tilde{g}^2 b)(a(\tilde{g}^2M_Z^2 - 2e^2b) + 2e^2M_A^4\chi^2)}}{M_V^2 a(4e^2 + \tilde{g}^2(b - M_Z^2)) - M_A^4\chi^2(2e^2M_Z^2 + \tilde{g}^2 b))}}, \tag{A25}$$

$$g1 = \tilde{g}\sqrt{\frac{(\tilde{g}^2 - 2e^2)abM_Z^2 - \sqrt{abM_Z^2(2e^2M_Z^2 + \tilde{g}^2 b)(a(\tilde{g}^2M_Z^2 - 2e^2b) + 2e^2M_A^4\chi^2)}}{M_V^2 a(4e^2 + \tilde{g}^2(b - M_Z^2)) - M_A^4\chi^2(2e^2M_Z^2 + \tilde{g}^2 b))}}, \tag{A26}$$

where $a = (M_A^2 - M_Z^2)$, $b = (M_V^2 - M_Z^2)$, and we have not replaced M_V and χ, as they are purely functions of the independent parameters and not of either g_1 or g_2.

4. Effect of S on Z'/Z'' properties

Here we provide the additional figures and information relevant to the phenomenological study presented in this paper. Throughout the paper we have chosen $S = 0.1$ and $s = 0$ as the benchmark parameter space values, and the effect of varying S is discussed here. As s is the Lagrangian parameter that quantifies Higgs interactions with the WTC gauge bosons, we continue to assume $s = 0$ throughout.

5. Mass spectra

Figures 12 and 13 present $M_{Z'}$ and $\Delta M/M_{Z'}$, respectively, for different values of S. The main feature to note is the mass inversion M_{inv} defined by Eq. (24) such that $M^2_{\text{inv}} \propto 1/S$. The inversion point with $\Delta \simeq 0$ can be seen in Fig. 13 where the Z' is axial vector below the inversion point and vector above it. One can observe the inversion only for large values of $S = 0.2$ and 0.3 for the M_A around 2 and 1.6 TeV, respectively, according to Eq. (24).

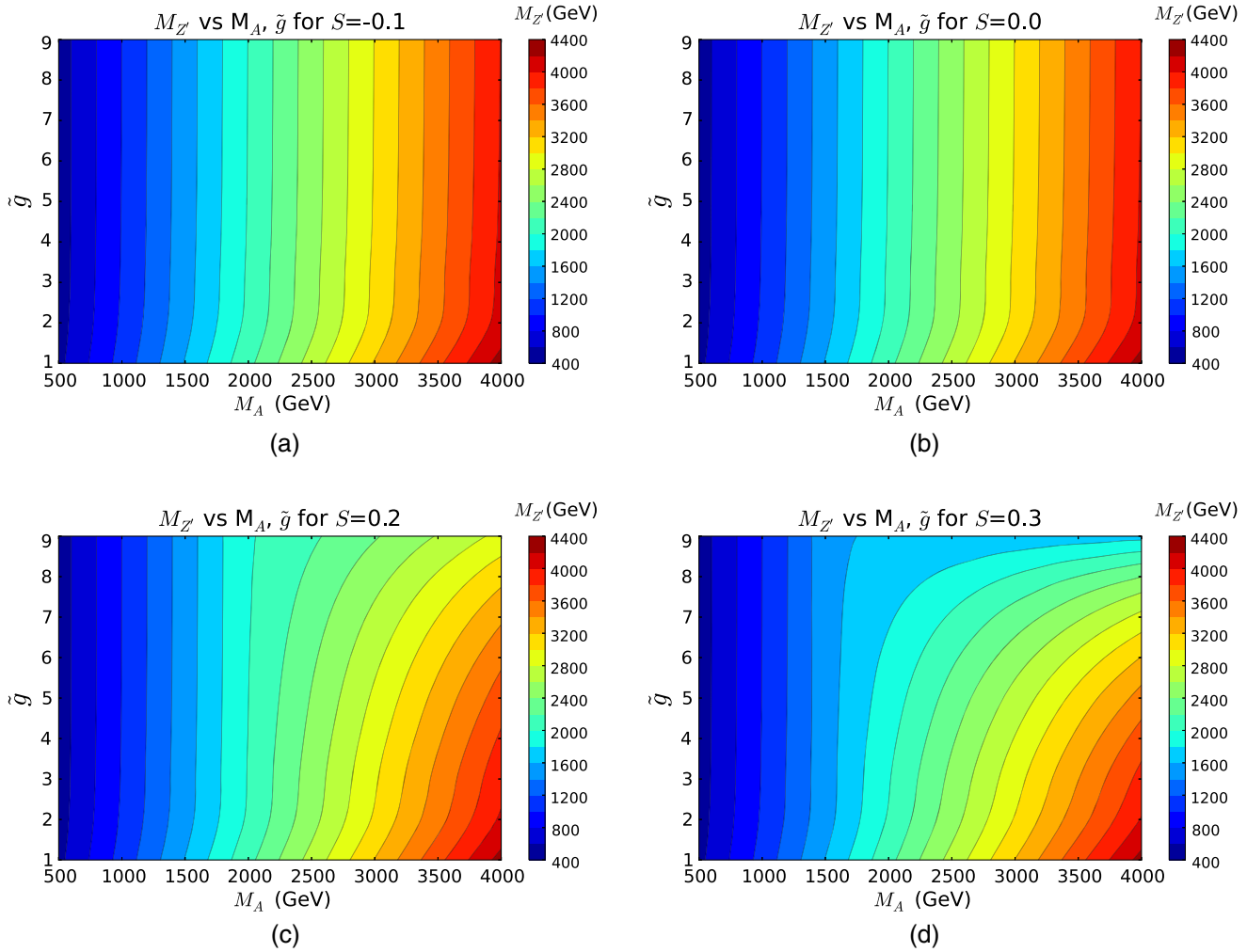

FIG. 12. $M_{Z'}$ (GeV) as a function of M_A and $\tilde{g}$ parameters for the fixed values of (a) $S = -0.1$, (b) $S = 0.0$, (c) $S = 0.2$, and (d) $S = 0.3$, respectively, and $s = 0$ throughout.

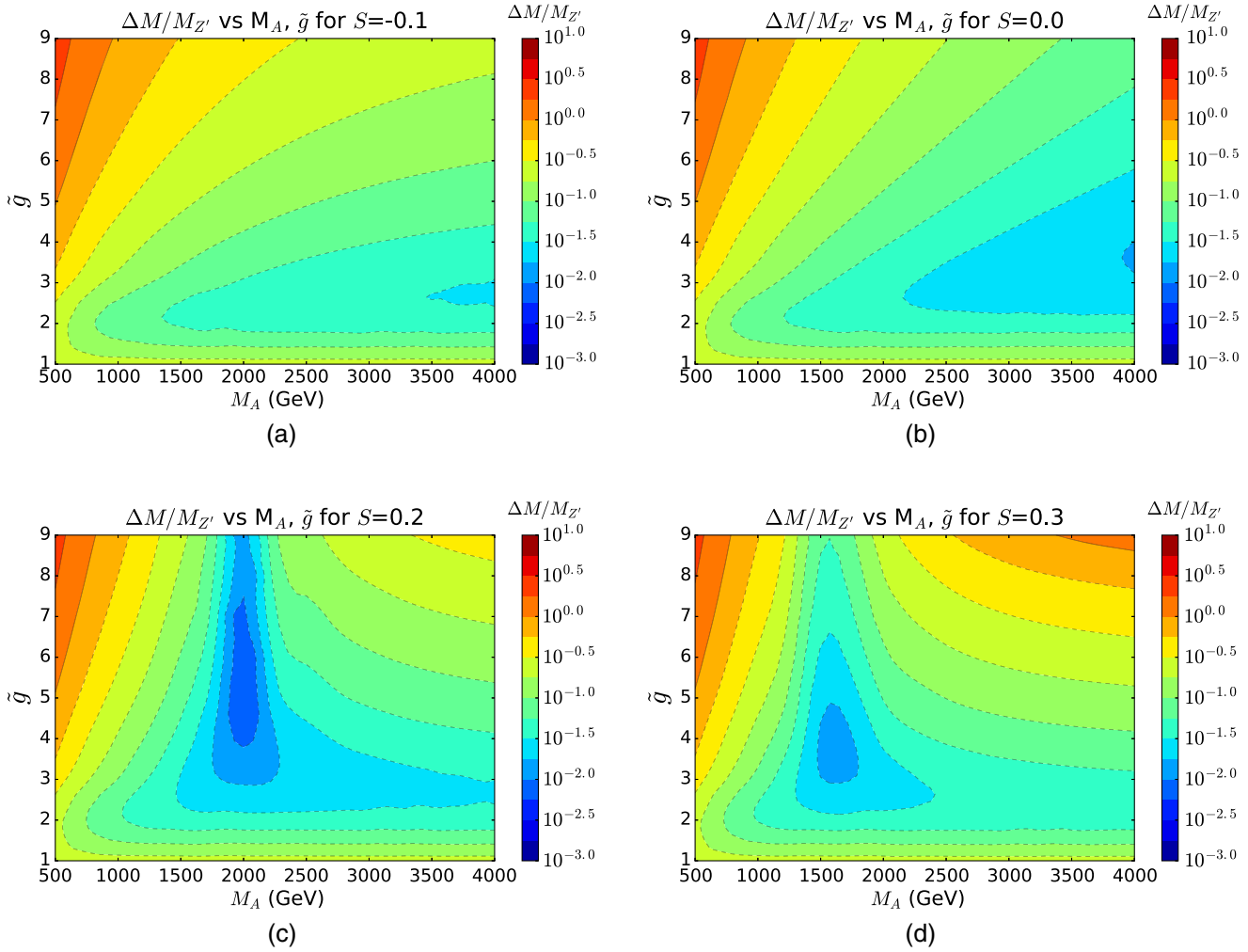

FIG. 13. $\Delta M/M_{Z'}$ as a function of M_A and $\tilde{g}$ parameters for the fixed values of (a) $S = -0.1$, (b) $S = 0.0$, (c) $S = 0.2$, and (d) $S = 0.3$, respectively, and $s = 0$ throughout.

a. Couplings

In Figs. 14–17 we present the L-R components of the dilepton couplings for the Z' and Z'', respectively, for different values of S. These are analogous to the couplings presented in Sec. III A 2, where the analytic form for the coupling components are also presented. The S dependence of these couplings is implicit in χ, g_1, and g_2, and the effect on the parameter space dependence for varying S is presented here.

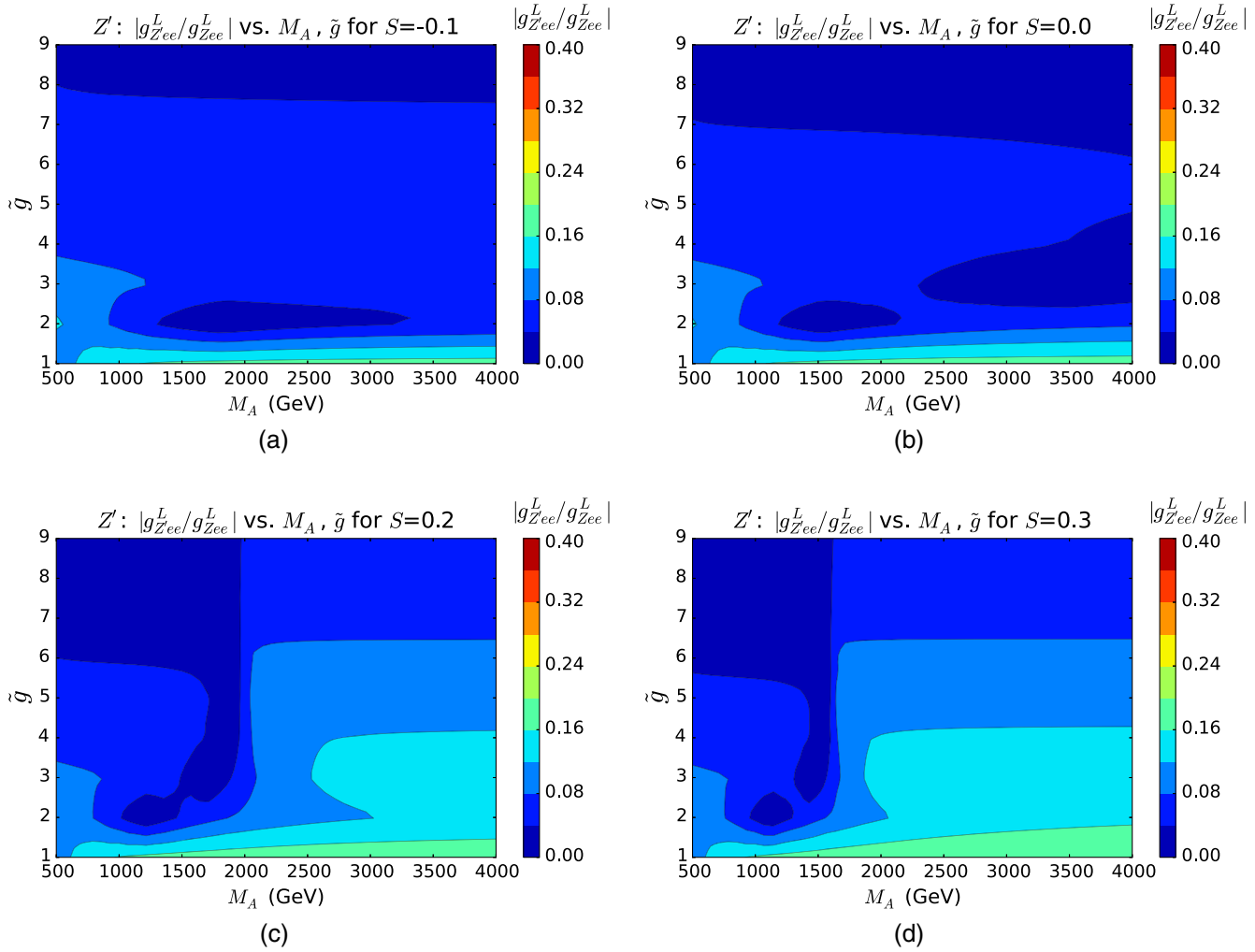

FIG. 14. Left-handed component of the coupling of Z' to charged lepton pairs as a ratio to its SM equivalent, $|g_{Z'l^+l^-}/g_{Zl^+l^-}|$, as a function of M_A and $\tilde{g}$ parameters for the fixed values of (a) $S = -0.1$, (b) $S = 0.0$, (c) $S = 0.2$, and (d) $S = 0.3$, respectively.

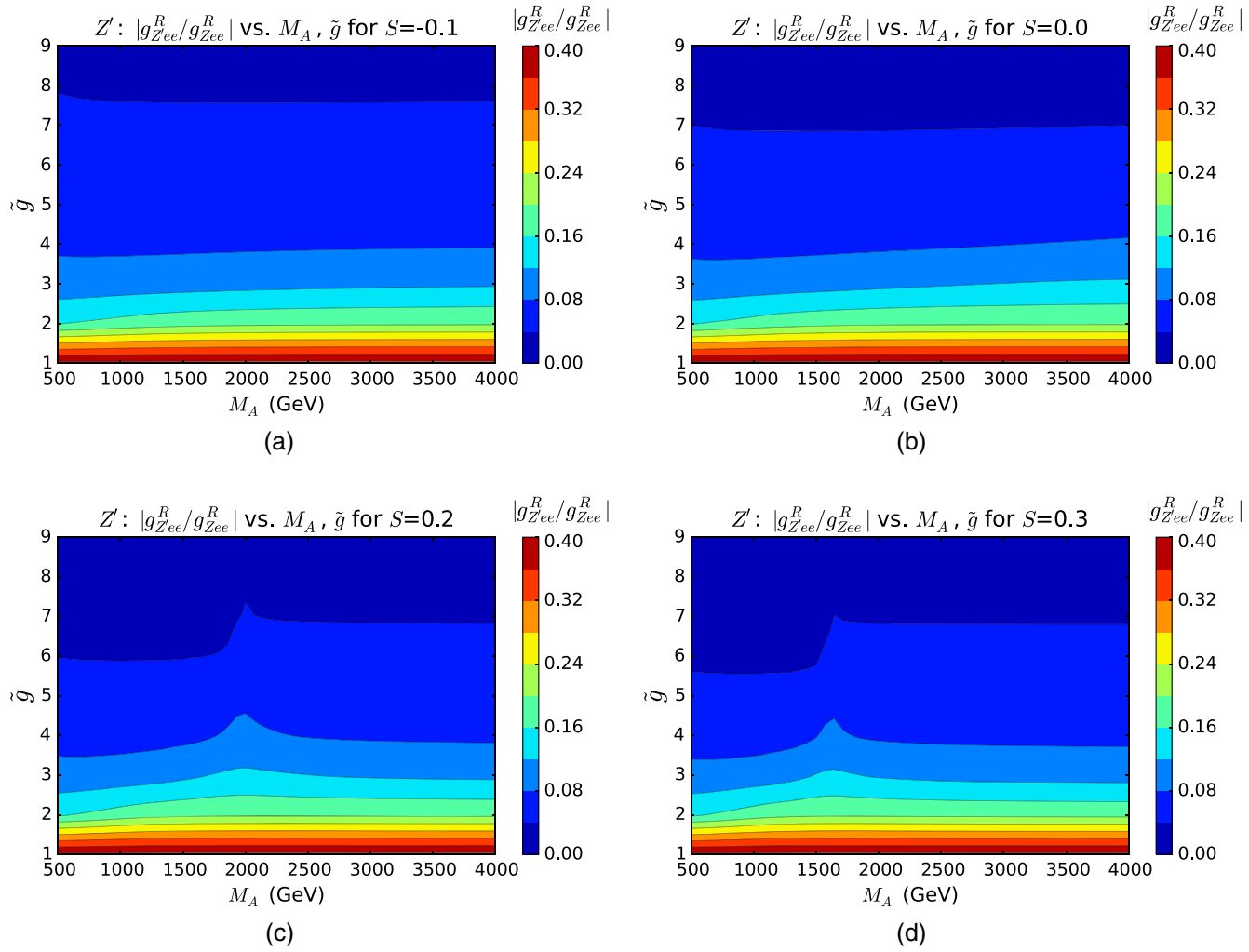

FIG. 15. Right-handed component of the coupling of Z' to charged lepton pairs as a ratio to its SM equivalent, $|g_{Z'l^+l^-}/g_{Zl^+l^-}|$, as a function of M_A and $\tilde{g}$ parameters for the fixed values of (a) $S = -0.1$, (b) $S = 0.0$, (c) $S = 0.2$, and (d) $S = 0.3$, respectively.

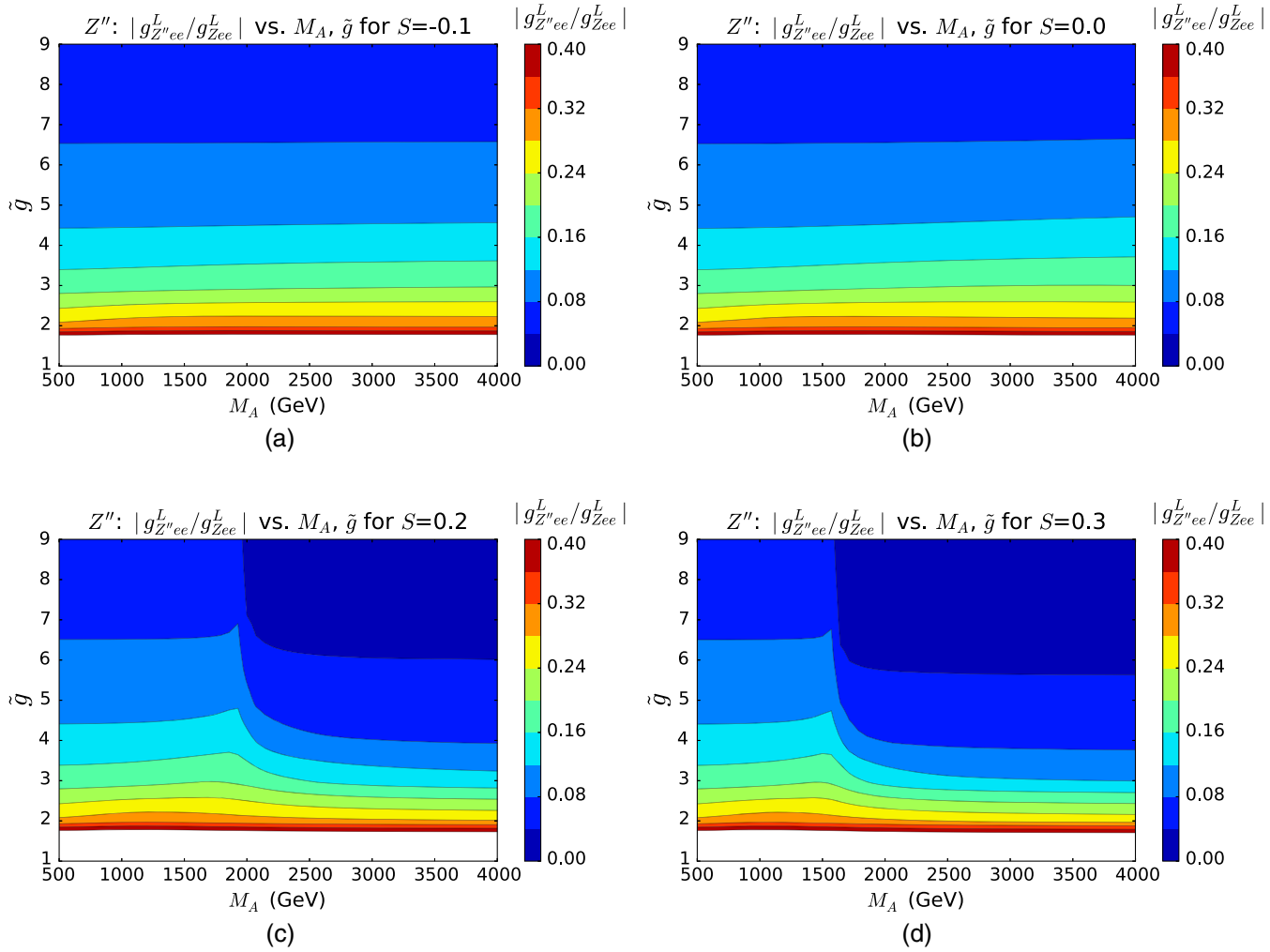

FIG. 16. Left-handed component of the coupling of Z'' to charged lepton pairs as a ratio to its SM equivalent, $|g_{Z''l^+l^-}/g_{Zl^+l^-}|$, as a function of M_A and $\tilde{g}$ parameters for the fixed values of (a) $S = -0.1$, (b) $S = 0.0$, (c) $S = 0.2$, and (d) $S = 0.3$, respectively.

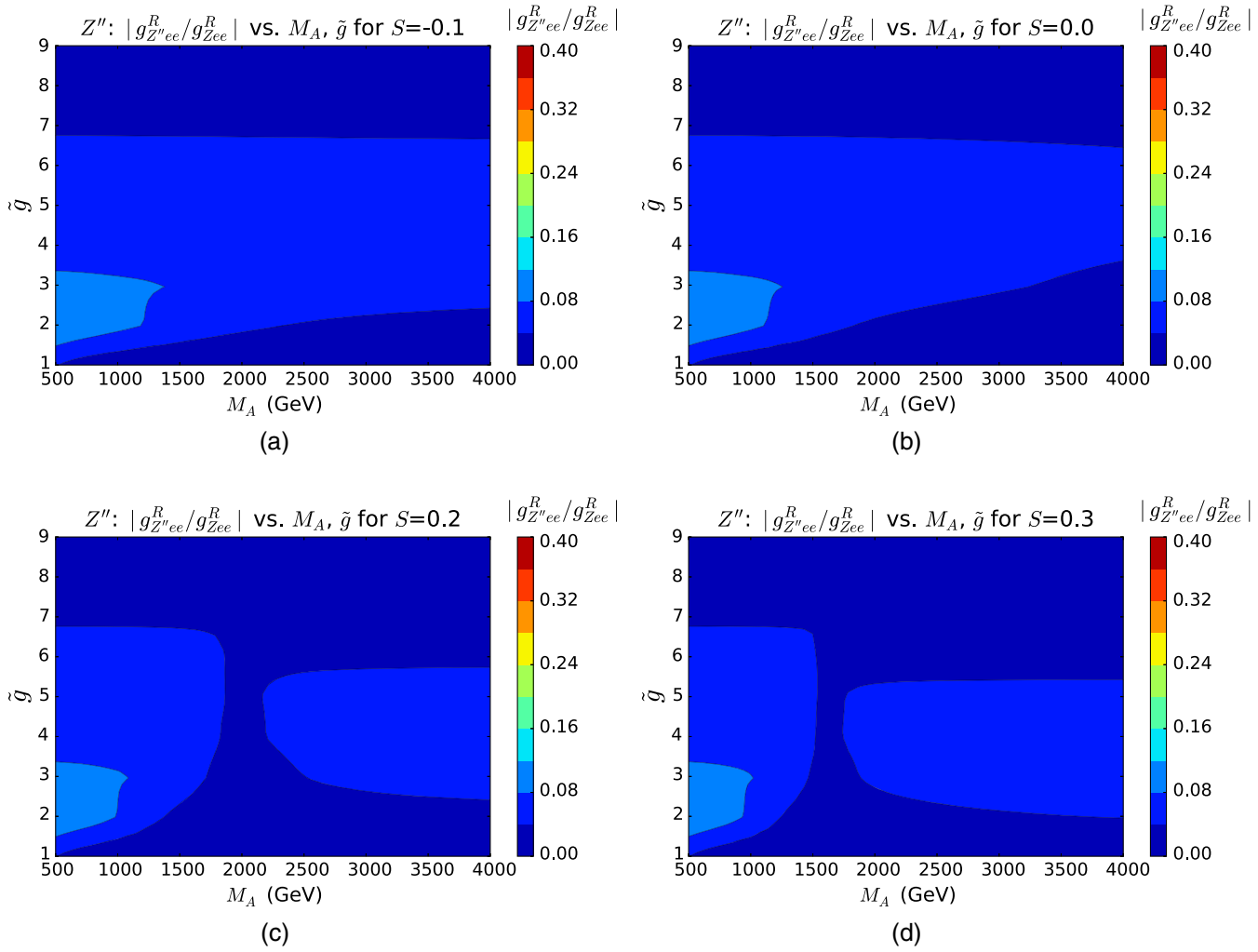

FIG. 17. Right-handed component of the coupling of Z'' to charged lepton pairs as a ratio to its SM equivalent, $|g_{Z''l^+l^-}/g_{Zl^+l^-}|$, as a function of M_A and $\tilde{g}$ parameters for the fixed values of (a) $S = -0.1$, (b) $S = 0.0$, (c) $S = 0.2$, and (d) $S = 0.3$, respectively.

b. Widths and branching ratios

The width-to-mass ratio for Z' and Z'' for different S are shown in Figs. 18 and 19. The widths largely show similar behavior to those at the benchmark value of $S = 0.1$ (Fig. 5), with the exception of $S = 0$. At $S = 0$, the Z' width-to-mass ratio is very small (less than % level), so the Z' resonance is always narrow at this S. The Z'' also has a narrower width for much of the parameter space at $S = 0$; however, the region of $\Gamma_{Z''} \geq M_{Z''}$ nevertheless appears in the region with low M_A and high $\tilde{g}$.

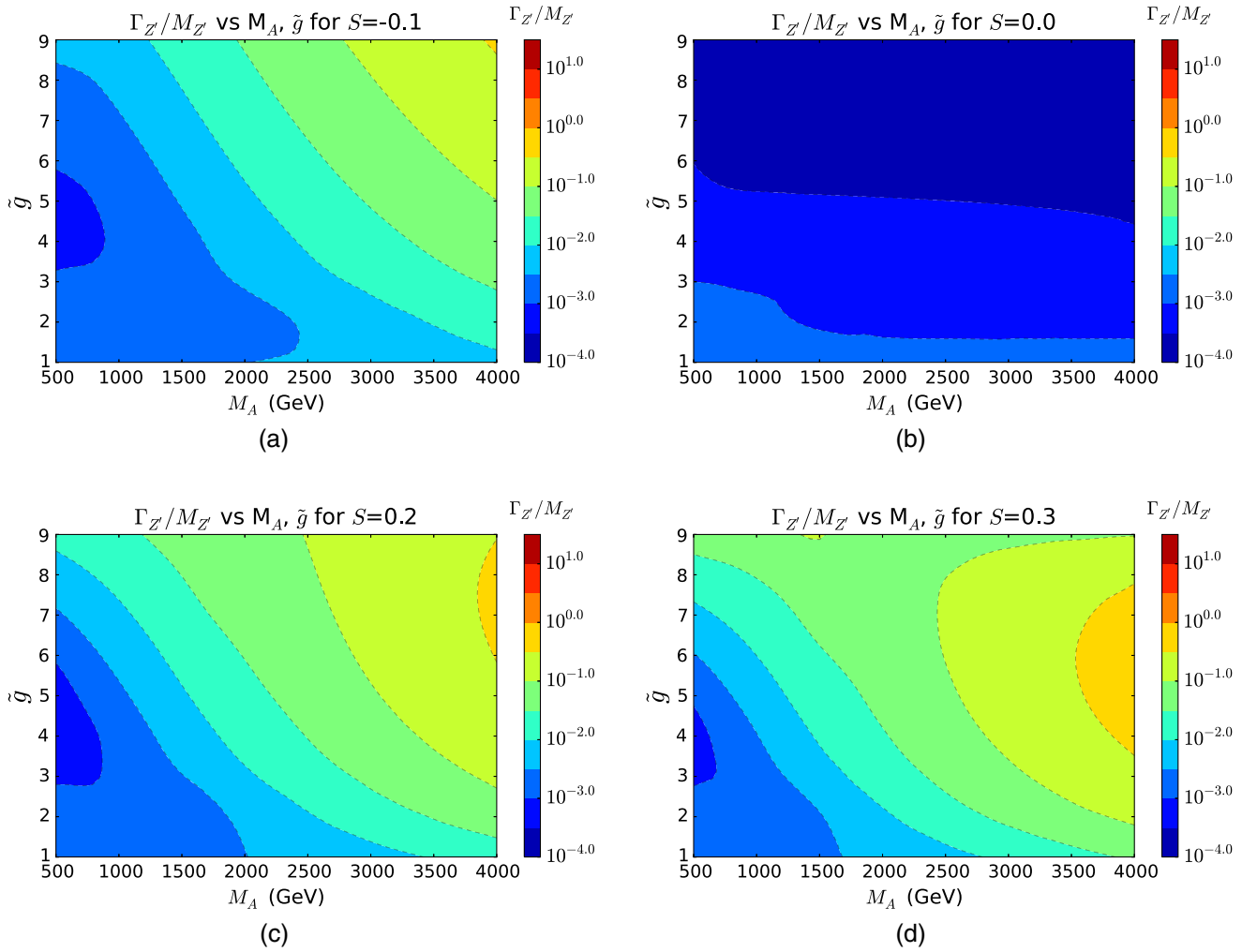

FIG. 18. $\Gamma_{Z'}/M_{Z'}$ as a function of M_A and $\tilde{g}$ parameters for the fixed values of (a) $S = -0.1$, (b) $S = 0.0$, (c) $S = 0.2$, and (d) $S = 0.3$, respectively.

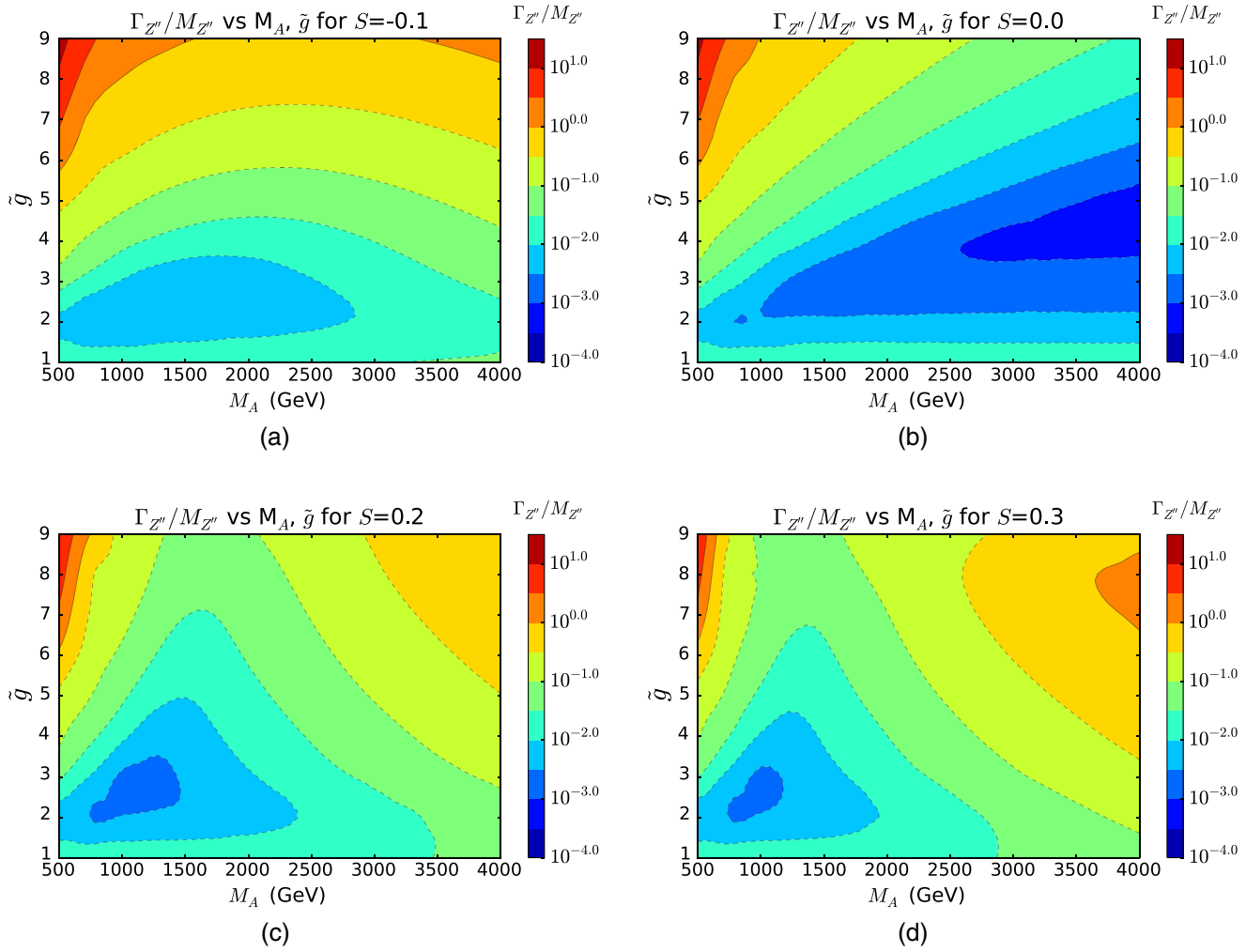

FIG. 19. $\Gamma_{Z''}/M_{Z''}$ as a function of M_A and $\tilde{g}$ parameters for the fixed values of (a) $S = -0.1$, (b) $S = 0.0$, (c) $S = 0.2$, and (d) $S = 0.3$, respectively.

The branching ratio spectra for the Z' with $\tilde{g} = 3, 8$ is presented in Figs. 20 and 21, and for the Z'' with $\tilde{g} = 3, 8$—in Figs. 22 and 23 for various values of S. The features of the branching ratio spectra such as the dips in the VV/Vh channels are discussed in Sec. III B, and again we note that the $Z'' \to W'^{+}W'^{-}$ channel is opened at low M_A, high $\tilde{g}$ at all values of S. Also note that for the Z', at $S = 0$ where the resonance is very narrow, the dilepton and diquark branching ratios are boosted and are the dominant decay channels across the whole (M_A, $\tilde{g}$) parameter space.

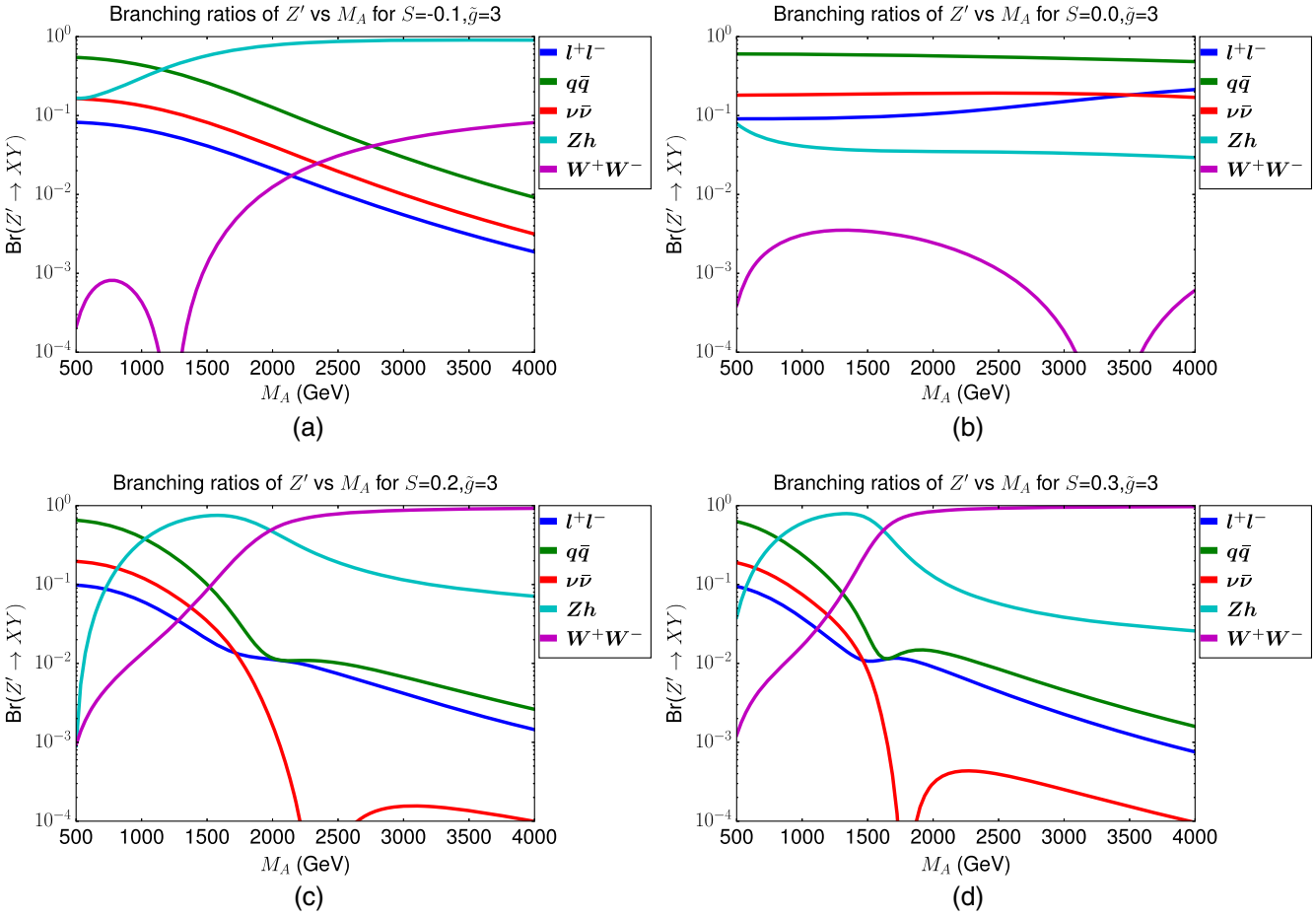

FIG. 20. Br(Z') for all decay channels as a function of M_A at fixed value of $\tilde{g} = 3$ for (a) $S = -0.1$, (b) $S = 0.0$, (c) $S = 0.2$, and (d) $S = 0.3$, respectively.

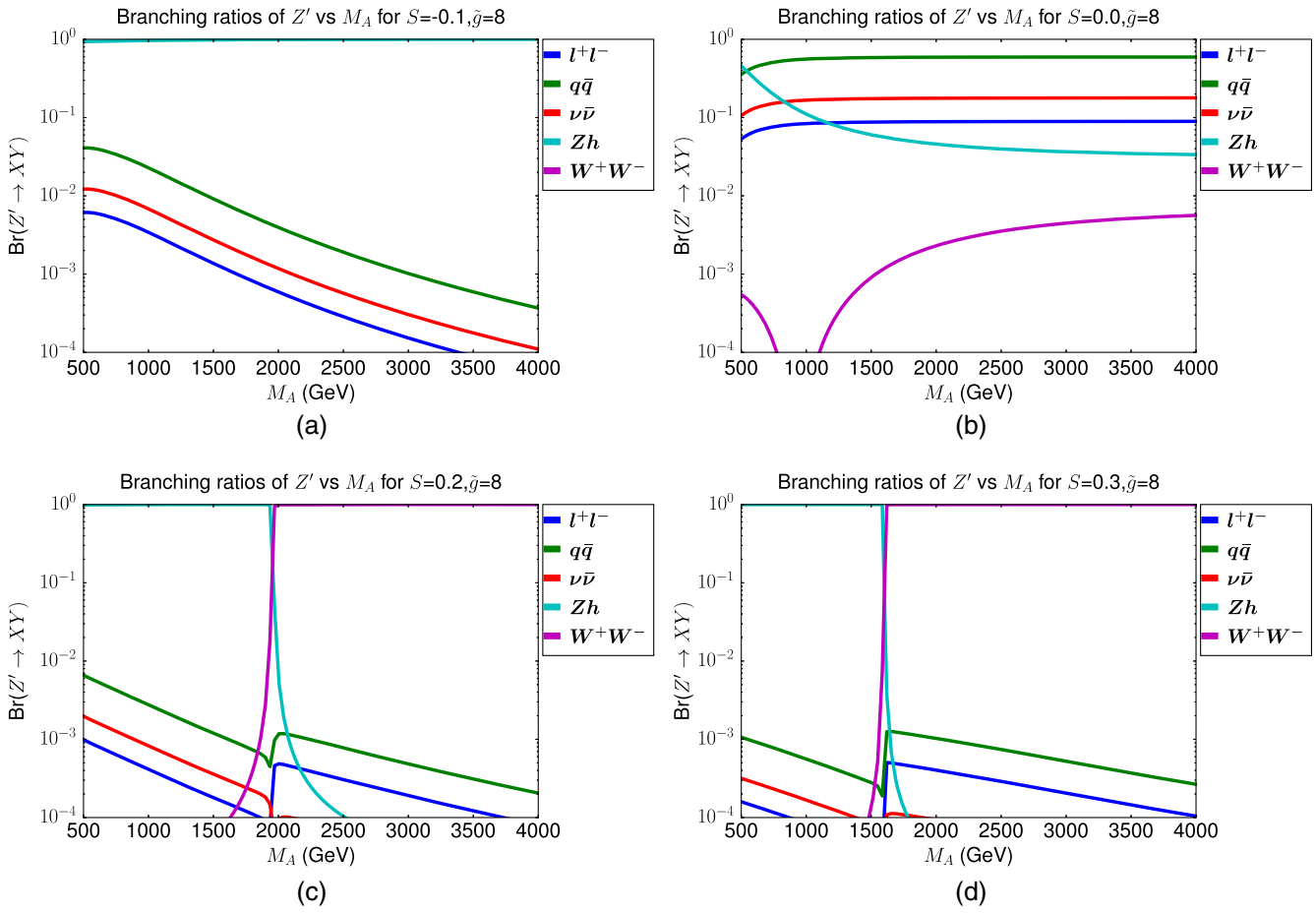

FIG. 21. $\mathrm{Br}(Z')$ for all decay channels as a function of M_A at fixed value of $\tilde{g} = 8$ for (a) $S = -0.1$, (b) $S = 0.0$, (c) $S = 0.2$, and (d) $S = 0.3$, respectively.

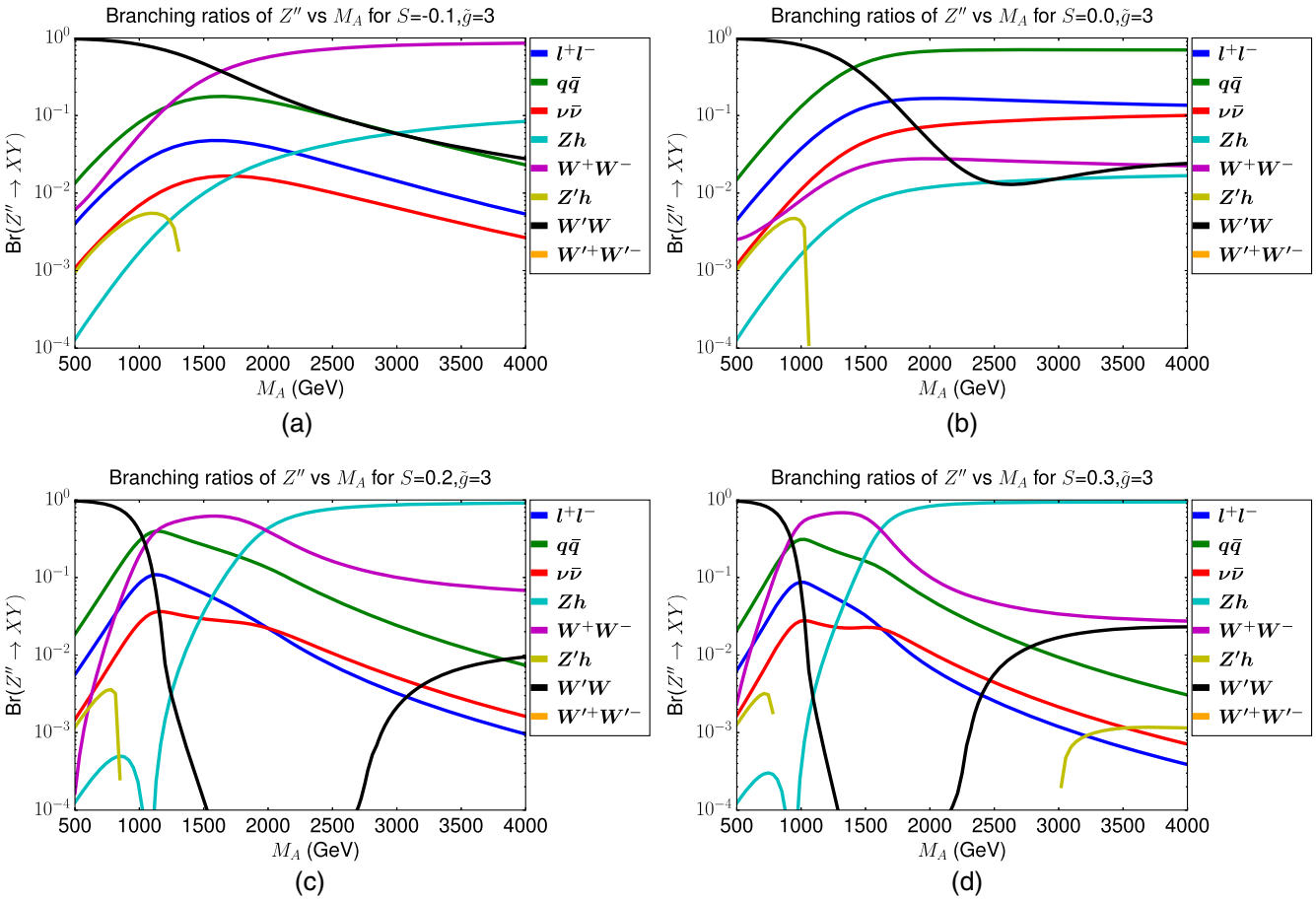

FIG. 22. $\mathrm{Br}(Z'')$ for all decay channels as a function of M_A at fixed value of $\tilde{g} = 3$ for (a) $S = -0.1$, (b) $S = 0.0$, (c) $S = 0.2$, and (d) $S = 0.3$, respectively.

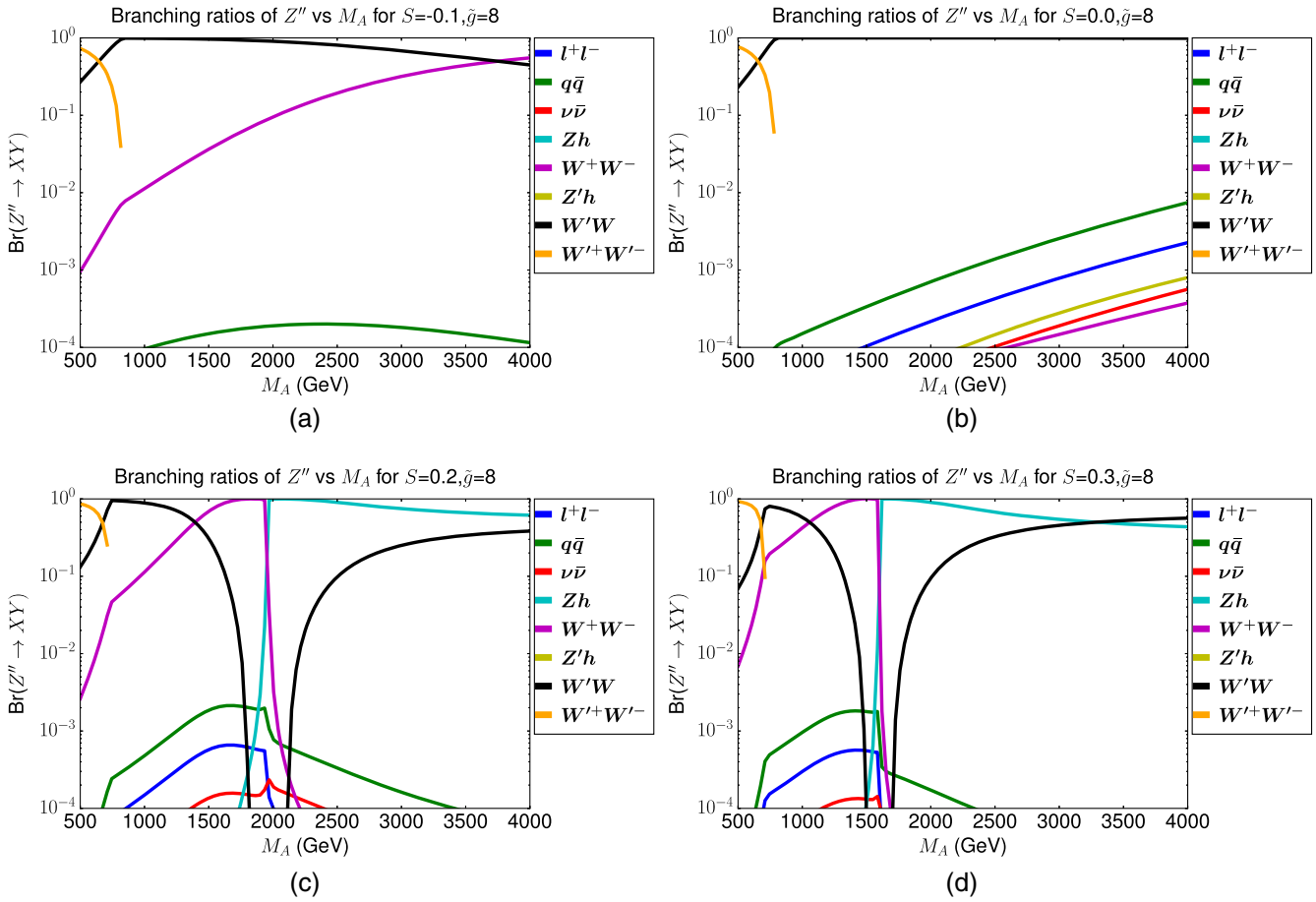

FIG. 23. Br(Z'') for all decay channels as a function of M_A at fixed value of $\tilde{g} = 8$ for (a) $S = -0.1$, (b) $S = 0.0$, (c) $S = 0.2$, and (d) $S = 0.3$, respectively.

Again, the mass inversion point can also be identified as the point at which the W^+W^- and Zh branching ratios have a crossing point, hence the lack of crossing point at $S = -0.1,\ 0$.

c. Cross sections

The DY production cross sections at LO for $pp \to Z' \to e^+e^-$ $pp \to Z'' \to e^+e^-$ processes are presented in Figs. 24 and 25, respectively, as contour levels of the cross section in $(M_A, \tilde{g})$ space for different S.

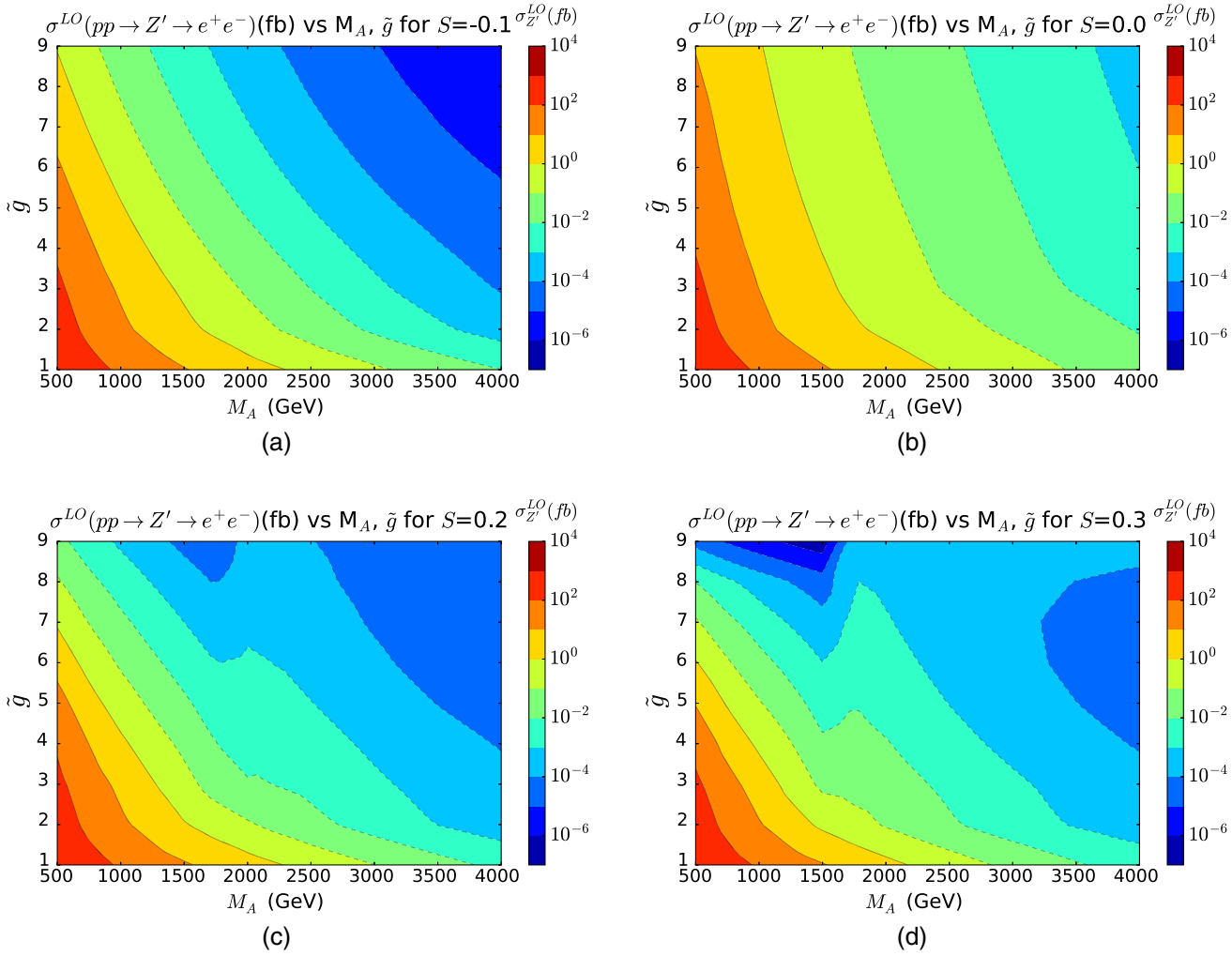

FIG. 24. DY production cross sections at LO for $pp \to Z' \to e^+e^-$ for (a) $S = -0.1$, (b) $S = 0.0$, (c) $S = 0.2$, and (d) $S = 0.3$, respectively.

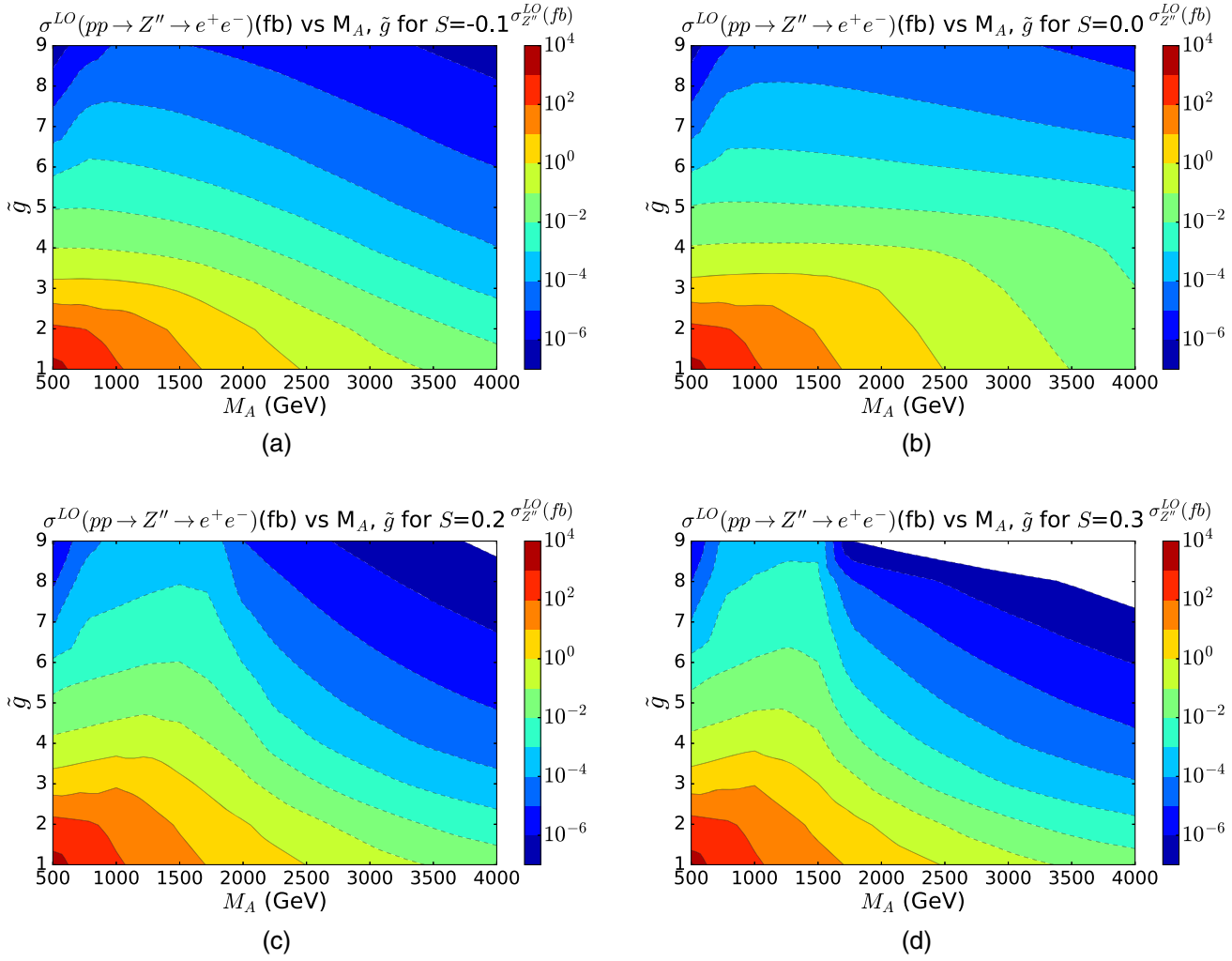

FIG. 25. DY production cross sections at LO for $pp \to Z'' \to e^+e^-$ for (a) $S = -0.1$, (b) $S = 0.0$, (c) $S = 0.2$, and (d) $S = 0.3$, respectively.

6. Effect of S on parameter space exclusions

As noted in Sec. IV, the S parameter could be of great importance in determining the excluded region of WTC parameter space. As such, we present a set of figures for each discrete S in which we show the current and future limits on the WTC parameter space for fixed S. This is for direct comparison to the exclusions quoted and discussed in Sec. III E 2. Figures 26–29 show the excluded regions of M_A, $\tilde{g}$ for $S = -0.1$, 0, 0.2, 0.3, respectively.

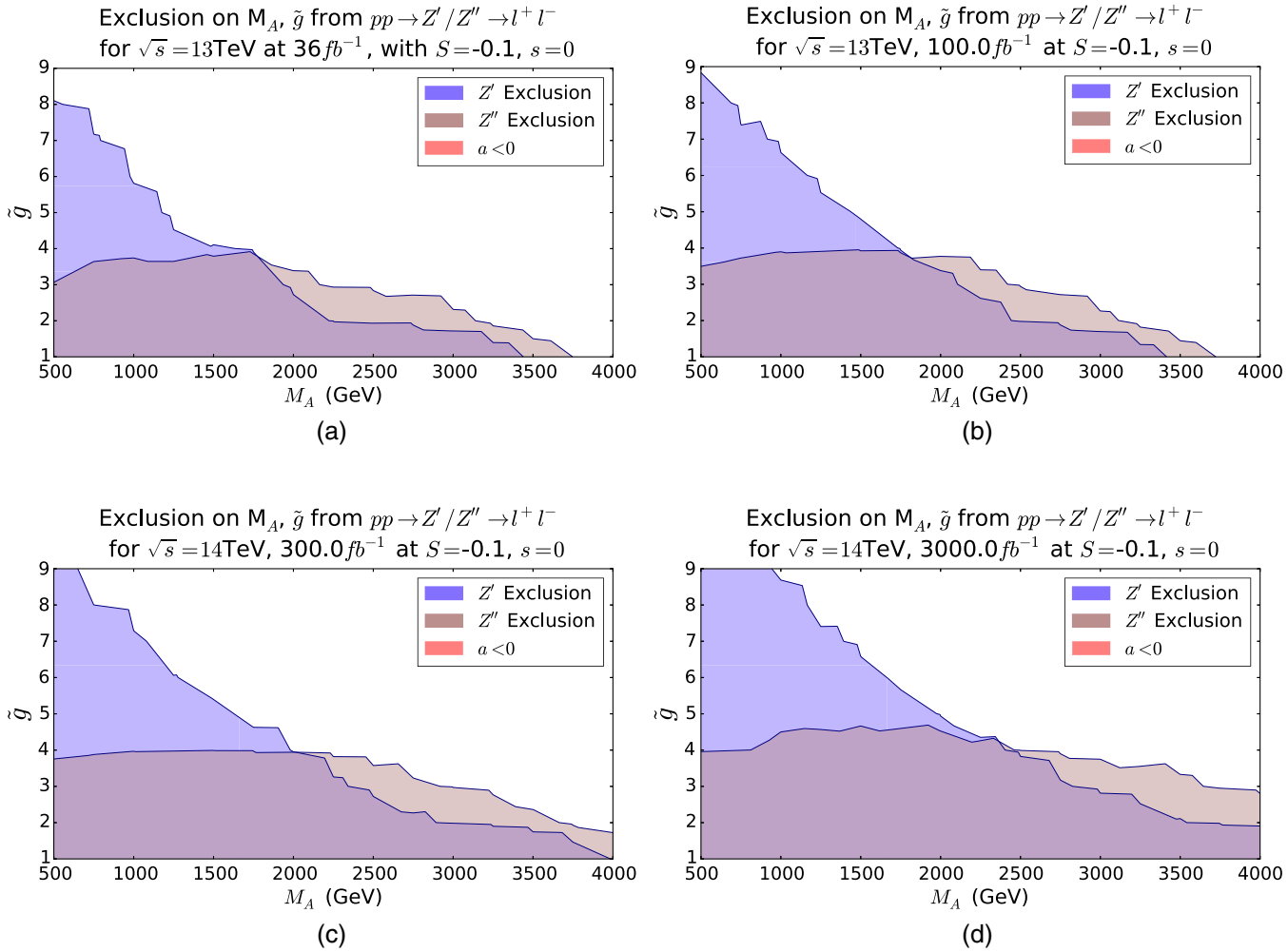

FIG. 26. Exclusion of the M_A,$\tilde{g}$ parameter space from Z' and Z'' DY processes at $\sqrt{s} = 13$ TeV and luminosity of 36 fb^{-1} (a). Predicted exclusion regions for the NMWT parameter space at (a) $\sqrt{s} = 13$ TeV and $\mathcal{L} = 100$ fb^{-1}, (b) $\sqrt{s} = 14$ TeV and $\mathcal{L} = 300$ fb^{-1}, and (c) $\sqrt{s} = 14$ TeV and $\mathcal{L} = 3000$ fb^{-1}.

The projected limits depend strongly on the S parameter, and for large S, the limit from dilepton searches at the LHC covers less of the parameter space, while the theoretical limit requiring $a > 0$ excludes a large portion of the M_A parameter space from above.

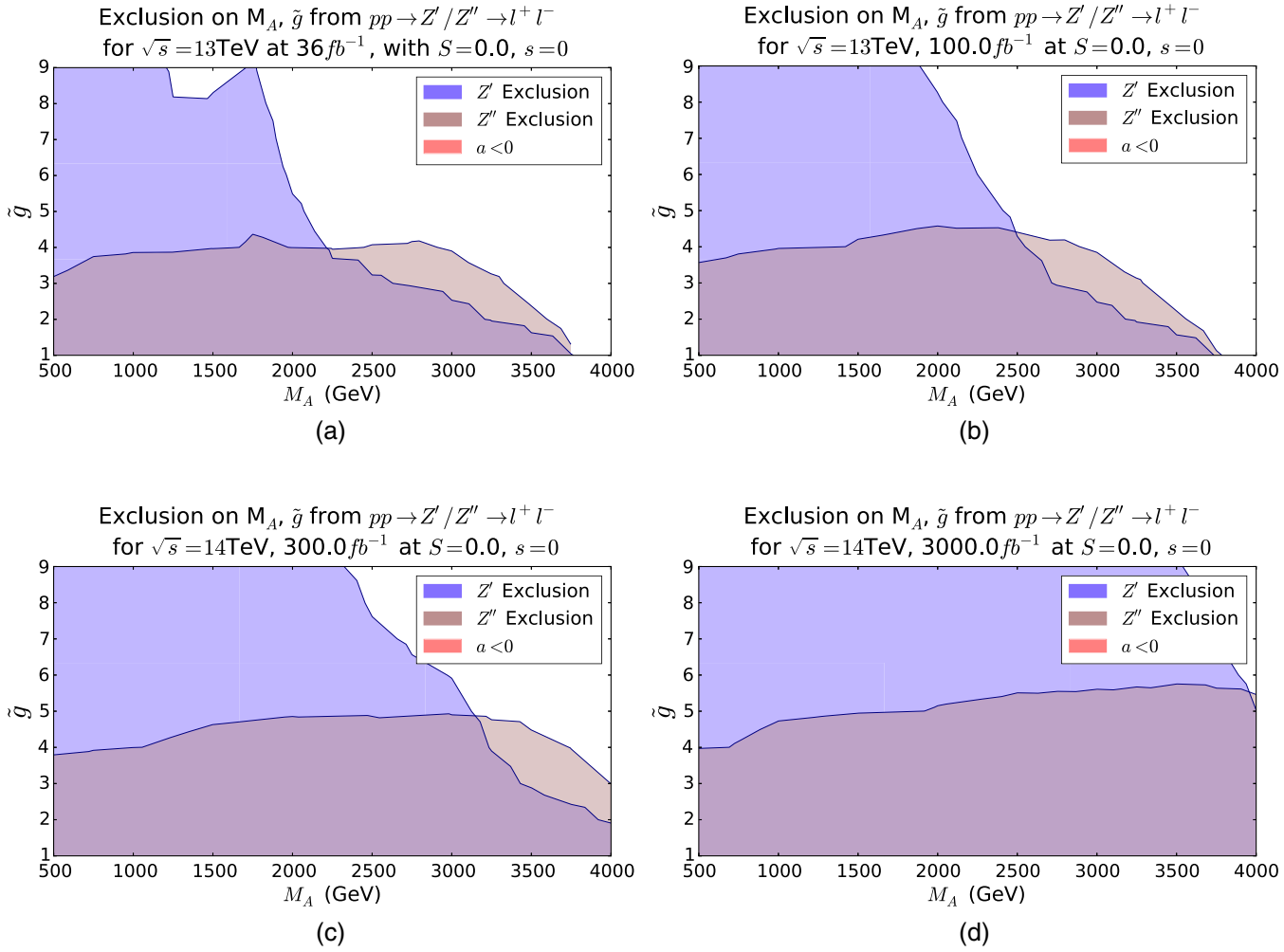

FIG. 27. Exclusion of the M_A,$\tilde{g}$ parameter space from Z' and Z'' DY processes at $\sqrt{s} = 13$ TeV and luminosity of 36 fb^{-1} (a). Predicted exclusion regions for the NMWT parameter space at (a) $\sqrt{s} = 13$ TeV and $\mathcal{L} = 100$ fb^{-1}, (b) $\sqrt{s} = 14$ TeV and $\mathcal{L} = 300$ fb^{-1}, and (c) $\sqrt{s} = 14$ TeV and $\mathcal{L} = 3000$ fb^{-1}.

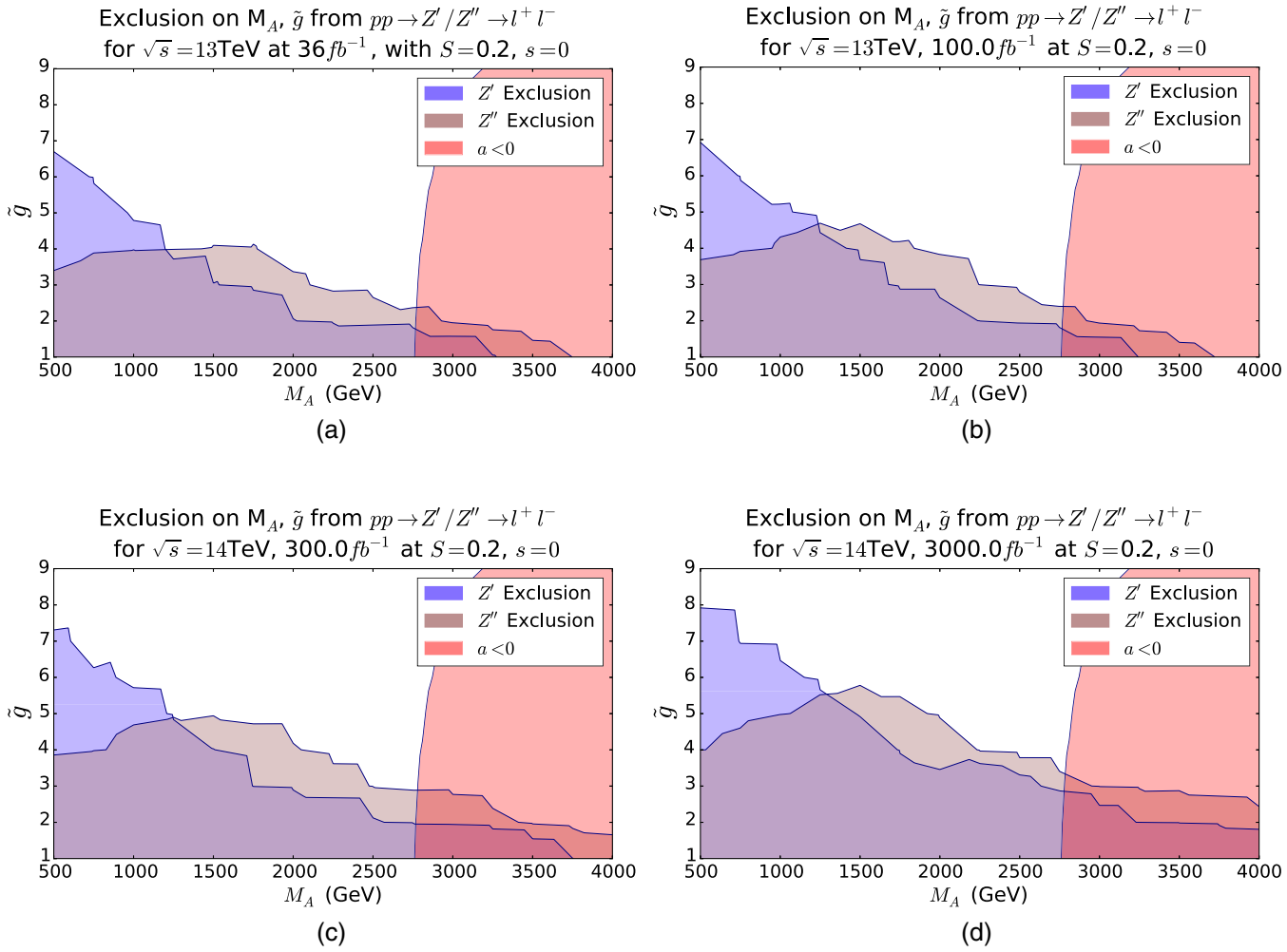

FIG. 28. Exclusion of the M_A,$\tilde{g}$ parameter space from Z' and Z'' DY processes at $\sqrt{s} = 13$ TeV and luminosity of 36 fb^{-1} (a). Predicted exclusion regions for the NMWT parameter space at (a) $\sqrt{s} = 13$ TeV and $\mathcal{L} = 100$ fb^{-1}, (b) $\sqrt{s} = 14$ TeV and $\mathcal{L} = 300$ fb^{-1}, and (c) $\sqrt{s} = 14$ TeV and $\mathcal{L} = 3000$ fb^{-1}.

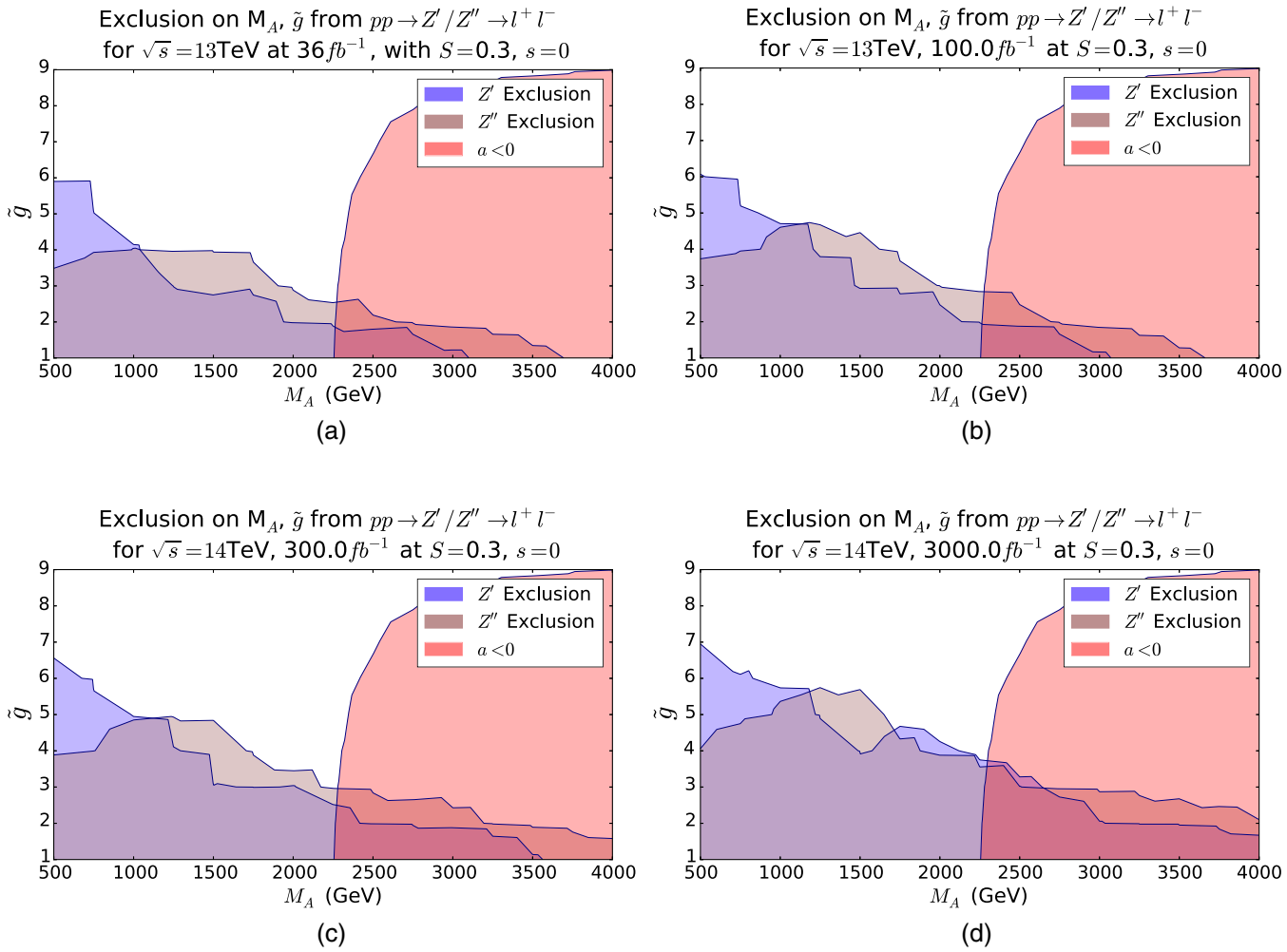

FIG. 29. Exclusion of the M_A,$\tilde{g}$ parameter space from Z' and Z'' DY processes at $\sqrt{s} = 13$ TeV and luminosity of 36 fb^{-1} (a). Predicted exclusion regions for the NMWT parameter space at (a) $\sqrt{s} = 13$ TeV and $\mathcal{L} = 100$ fb^{-1}, (b) $\sqrt{s} = 14$ TeV and $\mathcal{L} = 300$ fb^{-1}, and (c) $\sqrt{s} = 14$ TeV and $\mathcal{L} = 3000$ fb^{-1}.

[1] S. Chatrchyan *et al.* (CMS Collaboration), Observation of a new boson at a mass of 125 GeV with the CMS experiment at the LHC, Phys. Lett. B **716**, 30 (2012).

[2] G. Aad *et al.* (ATLAS Collaboration), Observation of a new particle in the search for the Standard Model Higgs boson with the ATLAS detector at the LHC, Phys. Lett. B **716**, 1 (2012).

[3] L. Susskind, Dynamics of spontaneous symmetry breaking in the weinberg-salam theory, Phys. Rev. D **20**, 2619 (1979).

[4] S. Weinberg, Implications of dynamical symmetry breaking, Phys. Rev. D **13**, 974 (1976); Phys. Rev. DErrattum **19**, 1277(A) (1979).

[5] M. E. Peskin and T. Takeuchi, Estimation of oblique electroweak corrections, Phys. Rev. D **46**, 381 (1992).

[6] S. King, A walk with technicolor, Phys. Lett. B **184**, 49 (1987).

[7] R. S. Chivukula, Weak Isospin Violation in 'Walking' Technicolor, Phys. Rev. Lett. **61**, 2657 (1988).

[8] S. F. King, Walking technicolor models, Nucl. Phys. **B320**, 487 (1989).

[9] T. Appelquist, Walking technicolor, in *International workshop on new trends in strong coupling gauge theories, Nagoya, Japan, 1988* (World Scientific Publishing Co, Teaneck, NJ, USA1988), p. 350, ISBN: 9971-50-846-X.

[10] R. Sundrum and S. D. H. Hsu, Walking technicolor and electroweak radiative corrections, Nucl. Phys. **B391**, 127 (1993).

[11] K. D. Lane and M. V. Ramana, Walking technicolor signatures at hadron colliders, Phys. Rev. D **44**, 2678 (1991).

[12] F. Sannino and K. Tuominen, Orientifold theory dynamics and symmetry breaking, Phys. Rev. D **71**, 051901 (2005).

[13] D. D. Dietrich and F. Sannino, Conformal window of SU(N) gauge theories with fermions in higher dimensional representations, Phys. Rev. D **75**, 085018 (2007).

[14] D. D. Dietrich, F. Sannino, and K. Tuominen, Light composite Higgs from higher representations versus electroweak precision measurements: Predictions for CERN LHC, Phys. Rev. D **72**, 055001 (2005).

[15] T. A. Ryttov and F. Sannino, Conformal windows of SU(N) Gauge theories, higher dimensional representations and the size of the unparticle world, Phys. Rev. D **76**, 105004 (2007).

[16] T. A. Ryttov and F. Sannino, Supersymmetry inspired QCD beta function, Phys. Rev. D **78**, 065001 (2008).

[17] F. Sannino, Dynamical stabilization of the Fermi scale: Phase diagram of strongly coupled theories for (Minimal) walking technicolor and unparticles, arXiv:0804.0182.

[18] R. Foadi, M. T. Frandsen, T. A. Ryttov, and F. Sannino, Minimal walking technicolor: Set up for collider physics, Phys. Rev. D **76**, 055005 (2007).

[19] R. Foadi, M. T. Frandsen, and F. Sannino, 125 GeV Higgs boson from a not so light technicolor scalar, Phys. Rev. D **87**, 095001 (2013).

[20] A. Belyaev, M. S. Brown, R. Foadi, and M. T. Frandsen, The technicolor Higgs in the light of LHC data, Phys. Rev. D **90**, 035012 (2014).

[21] G. Aad *et al.* (ATLAS Collaboration), Search for high-mass dilepton resonances in pp collisions at $\sqrt{s} =$ 8 TeV with the ATLAS detector, Phys. Rev. D **90**, 052005 (2014).

[22] G. Aad *et al.* (ATLAS Collaboration), Search for a new resonance decaying to a W or Z boson and a Higgs boson in the $\ell\ell/\ell\nu/\nu\nu + b\bar{b}$ final states with the ATLAS detector, Eur. Phys. J. C **75**, 263 (2015).

[23] A. Belyaev, R. Foadi, M. T. Frandsen, M. Jarvinen, F. Sannino, and A. Pukhov, Technicolor walks at the LHC, Phys. Rev. D **79**, 035006 (2009).

[24] D. B. Kaplan and H. Georgi, $SU(2) \times U(1)$ Breaking by Vacuum Misalignment, Phys. Lett. **136B**, 183 (1984).

[25] D. B. Kaplan, H. Georgi, and S. Dimopoulos, Composite Higgs scalars, Phys. Lett. **136B**, 187 (1984).

[26] J. A. Evans, J. Galloway, M. A. Luty, and R. A. Tacchi, Minimal conformal technicolor and precision electroweak tests, J. High Energy Phys. 10 (2010) 086.

[27] G. Cacciapaglia and F. Sannino, Fundamental composite (Goldstone) Higgs dynamics, J. High Energy Phys. 04 (2014) 111.

[28] J. Galloway, A. L. Kagan, and A. Martin, A UV complete partially composite-pNGB Higgs, Phys. Rev. D **95**, 035038 (2017).

[29] A. Agugliaro, O. Antipin, D. Becciolini, S. De Curtis, and M. Redi, UV complete composite Higgs models, Phys. Rev. D **95**, 035019 (2017).

[30] T. Alanne, D. Buarque Franzosi, and M. T. Frandsen, A partially composite Goldstone Higgs, Phys. Rev. D **96**, 095012 (2017).

[31] E. H. Simmons, Phenomenology of a technicolor model with heavy scalar doublet, Nucl. Phys. **B312**, 253 (1989).

[32] M. Dine, A. Kagan, and S. Samuel, Naturalness in supersymmetry, or raising the supersymmetry breaking scale, Phys. Lett. B **243**, 250 (1990).

[33] C. D. Carone, Technicolor with a 125 GeV Higgs Boson, Phys. Rev. D **86**, 055011 (2012).

[34] T. Alanne, S. Di Chiara, and K. Tuominen, LHC data and aspects of new physics, J. High Energy Phys. 01 (2014) 041.

[35] D. Buarque Franzosi, G. Cacciapaglia, H. Cai, A. Deandrea, and M. Frandsen, Vector and axial-vector resonances in composite models of the Higgs boson, J. High Energy Phys. 11 (2016) 076.

[36] M. Kurachi and R. Shrock, Study of the change from walking to non-walking behavior in a vectorial gauge theory as a function of N(f), J. High Energy Phys. 12 (2006) 034.

[37] Z. Fodor, K. Holland, J. Kuti, D. Nogradi, and C. H. Wong, Can a light Higgs impostor hide in composite gauge models?, Proc. Sci., LATTICE2013 (**2014**) 062.

[38] J. Kuti, The Higgs particle and the lattice, Proc. Sci., LATTICE2013 (**2014**) 004.

[39] P. Di Vecchia and G. Veneziano, Minimal composite higgs systems, Phys. Lett. **95B**, 247 (1980).

[40] T. Alanne, M. T. Frandsen, and D. Buarque Franzosi, Testing a dynamical origin of Standard Model fermion masses, Phys. Rev. D **94**, 071703 (2016).

[41] T. Appelquist, P. S. Rodrigues da Silva, and F. Sannino, Enhanced global symmetries and the chiral phase transition, Phys. Rev. D **60**, 116007 (1999).

[42] M. Bando, T. Kugo, and K. Yamawaki, Nonlinear realization and hidden local symmetries, Phys. Rep. **164**, 217 (1988).

[43] S. Weinberg, Precise Relations between the Spectra of Vector and Axial-Vector Mesons, Phys. Rev. Lett. **18**, 507 (1967).

[44] T. Appelquist and F. Sannino, The physical spectrum of conformal SU(N) gauge theories, Phys. Rev. D **59**, 067702 (1999).

[45] M. Kurachi and R. Shrock, Behavior of the S parameter in the crossover region between walking and QCD-like regimes of an SU(N) gauge theory, Phys. Rev. D **74**, 056003 (2006).

[46] M. Baak, J. Cth, J. Haller, A. Hoecker, R. Kogler, K. Mnig, M. Schott, and J. Stelzer (Gfitter Group), The global electroweak fit at NNLO and prospects for the LHC and ILC, Eur. Phys. J. C **74**, 3046 (2014).

[47] A. Belyaev, N. D. Christensen, and A. Pukhov, CalcHEP 3.4 for collider physics within and beyond the Standard Model, Comput. Phys. Commun. **184**, 1729 (2013).

[48] A. V. Semenov, LanHEP: A Package for automatic generation of Feynman rules in field theory, Version 2.0, arXiv:hep-ph/0208011.

[49] J. Erler, P. Langacker, S. Munir, and E. R. Pena, Improved constraints on Z' bosons from electroweak precision data, J. High Energy Phys. 08 (**2009**) 017.

[50] M. Bondarenko, A. Belyaev, L. Basso, E. Boos, V. Bunichev *et al.*, High energy physics model database: Towards decoding of the underlying theory (within Les Houches 2011: Physics at TeV Colliders New Physics Working Group Report), arXiv:1203.1488.

[51] R. D. Ball, V. Bertone, S. Carrazza, L. Del Debbio, S. Forte, A. Guffanti, N. P. Hartland, and J. Rojo (NNPDF Collaboration), Parton distributions with QED corrections, Nucl. Phys. **B877**, 290 (2013).

[52] A. M. Sirunyan *et al.* (CMS Collaboration), Search for high-mass resonances in dilepton final states in proton-proton collisions at $\sqrt{s} = 13$ TeV, J. High Energy Phys. 06 (2018) 120.

[53] E. Accomando, D. Becciolini, A. Belyaev, S. Moretti, and C. Shepherd-Themistocleous, Z' at the LHC: Interference and finite width effects in Drell-Yan, J. High Energy Phys. 10 (2013) 153.

[54] R. Hamberg, W. L. van Neerven, and T. Matsuura, A Complete calculation of the order α_s^2 correction to the Drell-Yan K factor, Nucl. Phys. **B359**, 343 (1991).

[55] W. L. van Neerven and E. B. Zijlstra, The O (α_s^2) corrected Drell-Yan K factor in the DIS and MS scheme, Nucl. Phys. **B382**, 11 (1992).

[56] R. Hamberg, T. Matsuura, and W. van Neerven, ZWPROD program (1989–2002), http://www.lorentz.leidenuniv.nl/research/neerven/DECEASED/Welcome.html.

[57] A. Buckley, J. Ferrando, S. Lloyd, K. Nordstrm, B. Page, M. Rfenacht, M. Schnherr, and G. Watt, LHAPDF6: Parton density access in the LHC precision era, Eur. Phys. J. C **75**, 132 (2015).

[58] E. Accomando, A. Belyaev, L. Fedeli, S. F. King, and C. Shepherd-Themistocleous, Z' physics with early LHC data, Phys. Rev. D **83**, 075012 (2011).

[59] R. D. Ball *et al.*, Parton distributions with LHC data, Nucl. Phys. **B867**, 244 (2013).

[60] E. Accomando, D. Barducci, S. De Curtis, J. Fiaschi, S. Moretti, and C. H. Shepherd-Themistocleous, Drell-Yan production of multi Z-bosons at the LHC within non-universal ED and 4D composite Higgs models, J. High Energy Phys. 07 (2016) 068.

[61] P. Langacker, The physics of heavy Z' gauge bosons, Rev. Mod. Phys. **81**, 1199 (2009).

[62] P. Nath *et al.*, The hunt for new physics at the large hadron collider, Nucl. Phys. B, Proc. Suppl. **200–202**, 185 (2010).

[63] M. Aaboud *et al.* (ATLAS Collaboration), Search for new high-mass phenomena in the dilepton final state using 36 fb^1 of proton-proton collision data at $\sqrt{s} = 13$ TeV with the ATLAS detector, J. High Energy Phys. 10 (2017) 182.

[64] A. Belyaev, A. Coupe, E. Accomando, and D. Englert (to be published).